Article

Late Paleozoic Tectonics of the NW Tarim Block: Insights from Zircon Geochronology and Geochemistry in Xinjiang, China

Baozhong Yang [1,*], Ao Lv [2,*], Xiangrong Zhang [3], Yejin Zhou [1], Wenxiao Zhou [4] and Ernest Chi Fru [5]

1   School of Earth Sciences, China University of Geosciences, Wuhan 430074, China; yj_zhou@cug.edu.cn
2   Jiangsu Changjiang Geological Survey Institute, Nanjing 210046, China
3   Hubei Geological Research Laboratory, Wuhan 430034, China; zhangxiangrong180@163.com
4   Institute of Geological Survey, China University of Geosciences, Wuhan 430074, China; zhouwenxiao@cug.edu.cn
5   College of Physical and Engineering Sciences, School of Earth and Environmental Sciences, Centre for Geobiology and Geochemistry, Cardiff University, Cardiff CF10 3AT, Wales, UK; chifrue@cardiff.ac.uk
*   Correspondence: bzyang@cug.edu.cn (B.Y.); lvao_cjdz@163.com (A.L.); Tel.: +86-18907172826 (B.Y.)

Abstract: The Late Paleozoic strata on the northwestern margin of the Tarim Block provide valuable insights into the subduction and collision processes that formed the Southwest Tianshan Orogenic Belt. This study integrates detrital zircon U-Pb dating and sandstone geochemical analysis of the Balikelike and Kalundaer formations to examine sedimentary provenance and tectonic settings during the Cisuralian–Guadalupian Epoch in the Keping area on the northwestern margin of the Tarim Block. Three of five Precambrian detrital zircon U-Pb age populations, 2500–2300 and 2000–1800 Ma and 900–600 Ma, are likely related to the fragmentation of the Columbia supercontinent and Rodinia's assembly, respectively. Two Paleozoic detrital zircons, 500–380 Ma, are associated with Paleozoic magmatism. Among them, ~295 Ma zircons are associated with post-collisional extension and emplacement of the Tarim Large Igneous Province. Geochemical analysis of sandstones, coupled with tectonic reconstruction, indicates a passive continental margin setting in the northwestern margin of the Tarim Block during the Silurian Period, later transitioned to a foreland basin from the Pennsylvanian to the Guadalupian Epochs. The crustal transformation from the Middle-late Devonian to Early Mississippian marked the closure of the South Tianshan Ocean (STO), involving a soft collision and significant uplift, with major orogenesis occurring in the Late Guadalupian. Five key stages are identified in the evolution of the foreland basin: (1) Middle-late Devonian to Early Mississippian initiation (remnant ocean basin stage); (2) Late Mississippian to Early Pennsylvanian early stage; (3) Late Pennsylvanian to Early Cisuralian middle stage; (4) the Late Cisuralian stage; and (5) the terminal Guadalupian stage. These findings provide new constraints on when STO closed and propose an innovative foreland basin evolution model during the late post-collisional phase from the Late Mississippian to Guadalupian. Collectively, the data advance our understanding of the tectonic processes that shaped the northwestern Tarim Block, with broader implications for Paleozoic geodynamics.

Keywords: detrital zircon; U-Pb geochronology; the STO; Keping area; Tarim Block; tectonic setting; Guadalupian

1. Introduction

The Central Asian Orogenic Belt (CAOB) is one of the largest and longest-lived accretionary orogenic belts in the world [1–5], formed through multiple stages of amalgamation involving island arcs, oceanic islands, seamounts, accretionary wedges, and microcontinents [2,6–11]. It is situated between the Eastern European and Siberian Block to the north and the North China and Tarim Block to the south [2,6,12]. The South Tianshan orogenic belt (STOB), an important part of the CAOB, is located along the northwest margin of the

Tarim Basin. It extends from eastern Kyrgyzstan westward to the Gansu–Xinjiang junction in China. Structurally, the STOB lies between the Yili-Central Tianshan Block (YCTB) and the Tarim Block, with the Atbashy–Inylchek–South Nalati and Tarim faults to the north and south, respectively (Figure 1a,b). The STOB is composed of marine sedimentary, ophiolite fragments, ultrahigh/high-pressure metamorphic, intrusive, and volcanic rocks. It formed through a combination of the YCTB and the Tarim blocks after the closure of the STO [7,9,11,13–17]. Therefore, studying the tectonic evolution of the STOB is vital for understanding the processes of subduction and closure of the STO during the Paleozoic.
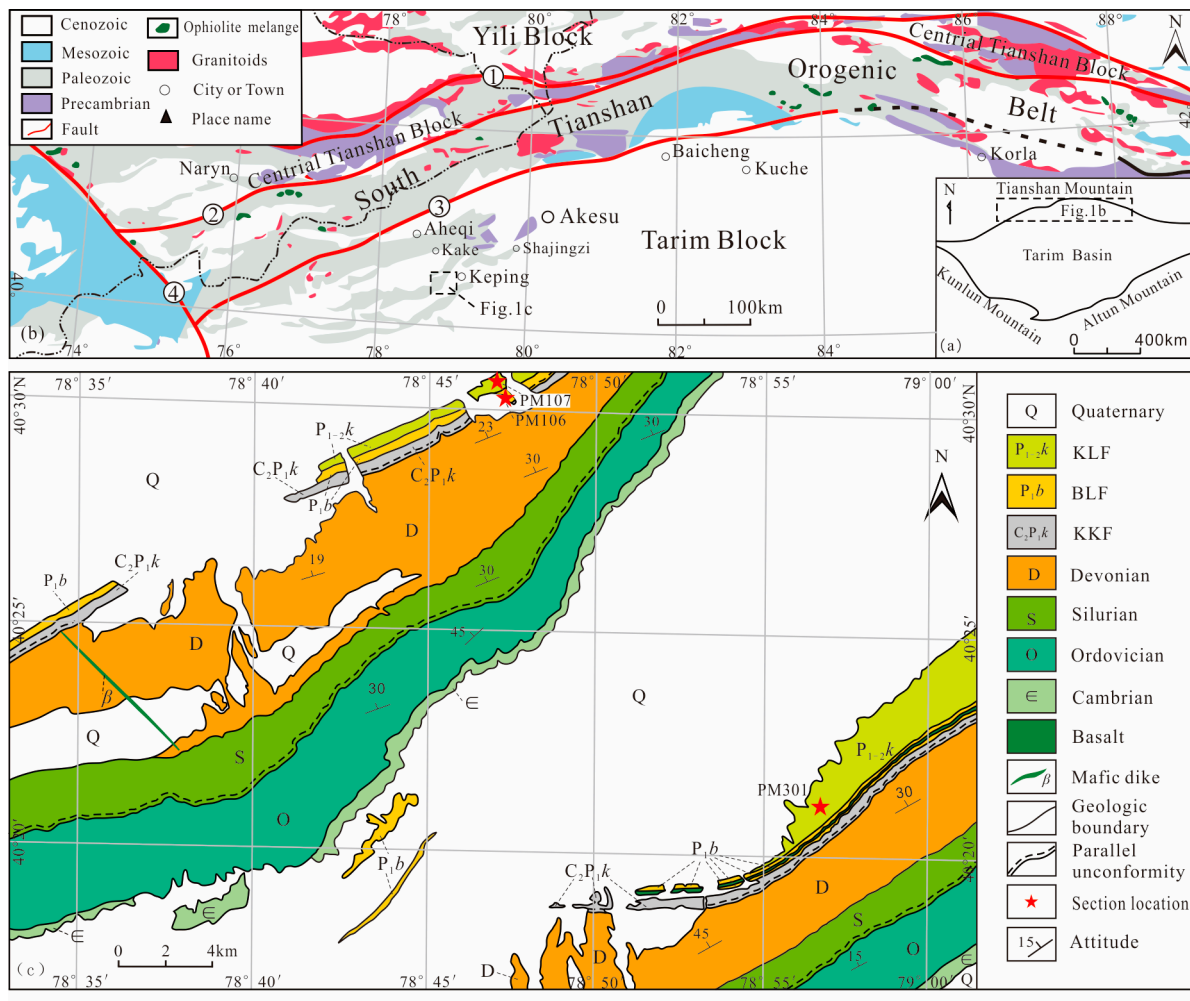

Figure 1. (**a**) Tectonic location of the study area; (**b**) tectonic geological map of the northern part of the Tarim Block, the western part of the STOB, and adjacent areas (Modified from Han (2015) [17]). Major faults: ① Nikolaev Line-North Nalati Fault; ② Atbashy–Inylchek–South Nalati Fault; ③ North Tarim Fault; ④ Talas–Ferghana Fault. (**c**) Geological map of the Keping area. KKF = Kangkelin Formation, comprising limestone, bioclastic limestone, calcareous sandstone, and mudstone; BLF = Balikelike Formation, comprising greyish limestone, grey-black bioclastic limestone, light grey-black mud-limestone, and an interbedded basalt layer; KLF = Kalundaer Formation, comprising lenticular conglomerates, calcareous sandstones, siltstones, and mudstones. (PM301-Section PM 301; PM106-Section PM106; PM107-Section PM107).

Although most researchers agree that the closure of the STO occurred as a scissor-like process from east to west during the Late Paleozoic [12], numerous crucial questions remain unresolved regarding the tectonic development of the STOB, particularly, the subduction polarity and the precise timing of the STO closure. There are mainly two types of subduction modes: unidirectional subduction and bidirectional subduction [6,13,18–22], among which

unidirectional subduction is further divided into southward subduction [14,23–26] and northward subduction [11,17,27–29]. Thus, the nature of the northern Tarim Block during the Paleozoic, active or passive, holds a pivotal role in understanding the subduction polarity of the STOB [30]. Moreover, the timing of the final closure of the STO is debated, with proposed timing from Late Devonian to Mississippian [31], Pennsylvanian [12,17,28], and Pennsylvanian to Cisuralian [28].

The northwestern margin of the Tarim Block hosts a well-preserved and complete Late Paleozoic stratigraphic sequence, offering insights into the evolution of orogenic belts. It serves as an important archive for understanding the tectonic history of the STOB [17,32–35]. Keping is located at the southern foot of the Tianshan Mountains in the western part of the Aksu region in Xinjiang, and its tectonic location belongs to the northwest margin of the Tarim Block (Figure 1). In this study, we analyzed three detrital zircon samples and the geochemistry of 21 Cisuralian–Guadalupian sandstones in the Keping area. Their corresponding sediment sources and tectonic settings were studied using these data to decipher magmatic events associated with adjacent orogenic belts. This contribution sheds light on the nature of the geodynamic evolution of the northern Tarim Block, the subduction polarity of the STO, and the timing of its closure.

2. Geological Backgrounds

The Tarim Block comprises the Archean–Neoproterozoic metamorphic basement and Paleozoic sedimentary rock cover. The Precambrian crystalline basement rocks are covered by early Paleozoic limestone, siliciclastic rocks, as well as late Paleozoic clastic and volcanic rocks. The Keping area, in the northwestern part of the Tarim Block adjacent to southwestern Tianshan, contains complete Paleozoic sedimentary records. The late Paleozoic sedimentary strata near Keping County, deformed by thin-skinned thrusting, consist of a series of parallel cuestas (Figure 1b,c).

The Upper Paleozoic strata in the Keping area consist of the Devonian and Carboniferous–Permian systems. The Devonian succession includes Yimugantawu ($D_{1–2}y$) and Keziertage Formation (D_3k), while the Carboniferous–Permian system includes the Kangkelin (C_2P_1k), Balikelike (P_1b), and Kalundaer Formation ($P_{1–2}k$). Except for an unconformity between the Carboniferous and the underlying strata, all other units are in conformable contact (Figure 2).

System/Period	Series/Epoch		Aheqi	Thk. (m)	Kake	Thk. (m)	Keping	Thk. (m)	Sedimentary environment
Permian	Lopingian								Denudation area
	Guadalupian		$P_{1–2}k$	1378	$P_{1–2}k$	>333	$P_{1–2}k$	>890	Delta
	Cisuralian		P_1b	641	P_1b	1085	P_1b	180	
Carboniferous	Pennsylvanian		C_2P_1k	1868	C_2P_1k	953	C_2P_1k	131	Open platform
			C_2b	364	C_2b	1408			
	Mississippian		C_1b	300	C_1b	>30			Alluvial fan
									Denudation area
Devonian	D_3		D_3k	428	D_3k	649	D_3k	1059	Delta
	$D_{1–2}$		$D_{1–2}y$	569	$D_{1–2}y$	137	$D_{1–2}y$	554	Tidal flat
Silurian	$S_{2–4}$		$S_{2–4}t$	196	$S_{2–4}t$	115	$S_{2–4}t$	205	Delta
	S_1		S_1k	545	S_1k	395	S_1k	504	

Figure 2. Stratigraphic division scheme and sedimentary environments in the Keping and adjacent areas. S_1k-Kepingtage Fm.; $S_{2–4}t$-Tataaiertage Fm.; C_1b-Bashisuogong Fm.; C_2b-Biegentawu Fm.; P_1ku-Kupukuziman Fm.; $P_{1–2}ka$-Kaipaizileike Fm.; P_2s-Shajingzi Fm. Fm. = Formation; Thk. = Thickness; Others shown in text. The horizontal lines in the diagram indicate isochrones, not thickness.

The main objective of this study is to examine the Cisuralian–Guadalupian strata in the Keping area. For this purpose, three sections were selected, located at Kepingtage Mountain (PM301) and Keziertage Mountain (PM106 and PM107) (Figures 1 and 3). The Cisuralian–Guadalupian successions are divided into the Balikelike and Kalundaer forma-

tions. The Balikelike Formation is characterized mainly by greyish limestone, grey-black bioclastic limestone, light grey-black mud-limestone, and an interbedded basalt layer, which is conformably overlain by the Kangkelin Formation (Figure 2). These lithological variations suggest deposition in a shallow-water environment within a mixed carbonate–clastic system. The Kalundaer Formation exhibits varied lithology, comprising lenticular conglomerates, calcareous sandstones, siltstones, and mudstones. Tree trunk fossils are preserved in the conglomerates, while low-angle crossbedding, water flow ripples, and sand ripple bedding are observed in the sandstones. The lithological features are shown in Figure 4. According to the rock composition, the Kalundaer Formation can be divided into three members: the First Member is a coastal-shallow marine deposit, the Second meandering river sedimentation, and the Third river-dominated delta sedimentation (Figure 3). Therefore, in the Cisuralian strata, the sedimentary environment in the study area is mainly shallow sea, with no significant changes. During the Late Cisuralian to Early-Guadalupian periods, there was a significant increase in sandstone composition, indicating the beginning of regression and river sedimentation. The mafic veins (Figure 5a–c) and basalt (Figure 5d–f) developed in the strata accurately constrain the age of this stratigraphic sequence to be later than 308 Ma, with an end time slightly later than 287.6 Ma [36], belonging to the Pennsylvanian to the Cisuralian interval.
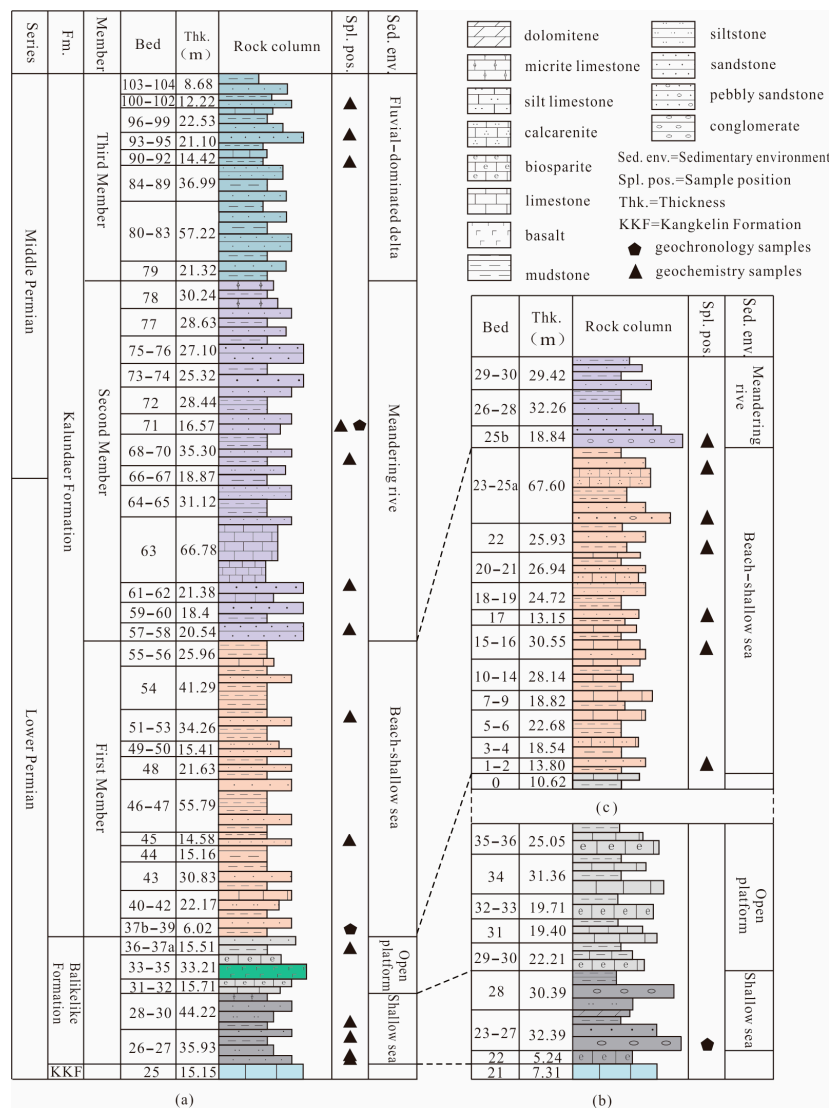

Figure 3. Sampling position in the stratigraphic column of the Cisuralian–Guadalupian Series in the study area. (**a**) Section PM301; (**b**) Section PM106; (**c**) Section PM107.
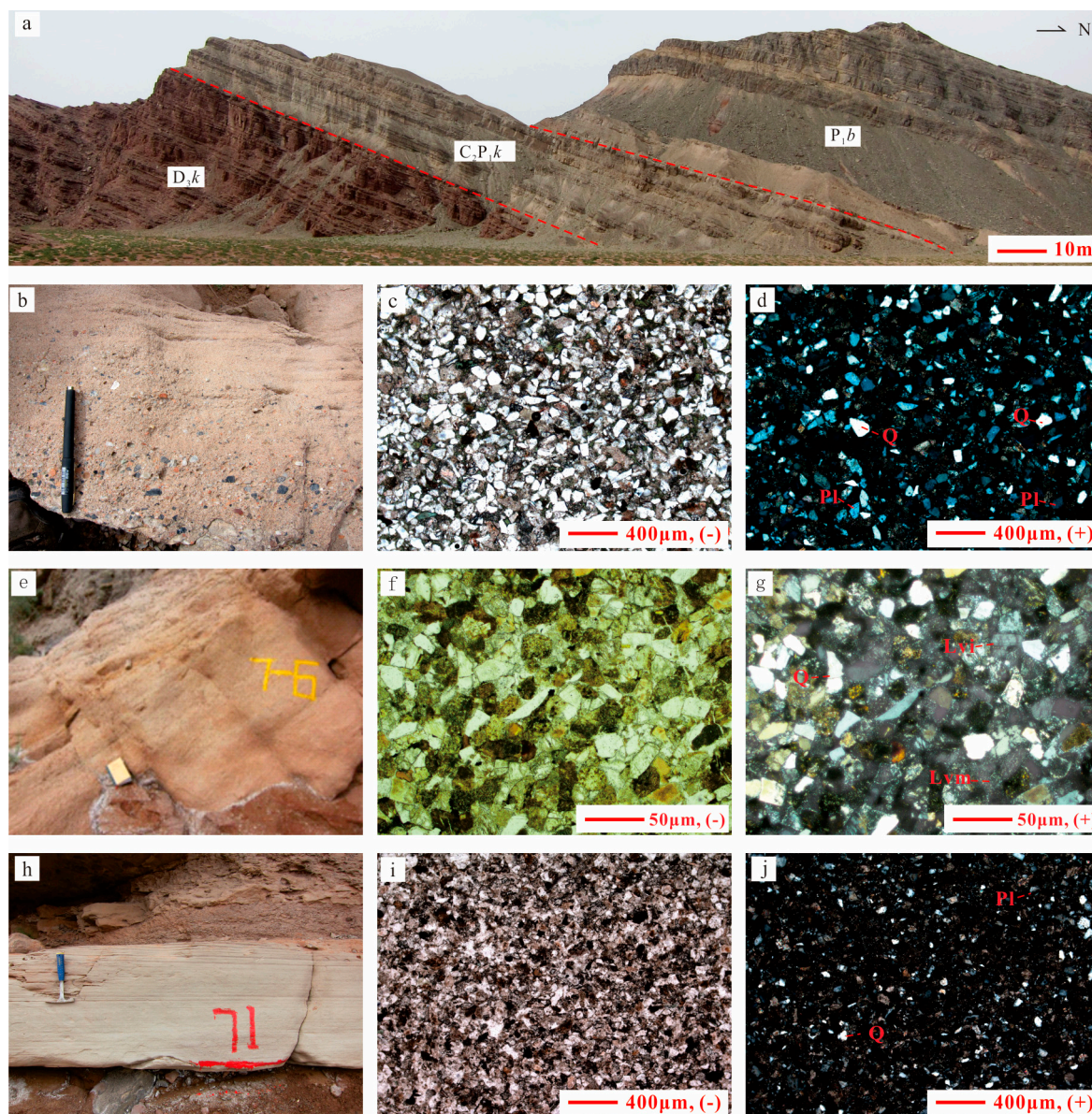
Figure 4. Lithological characteristics of the sandstone of the Balikelike and Kalundaer formations (**a**,**b**,**e**,**h**) Field photographs; Others are micrographs. (-) Under polarized light microscope; (+) Between crossed polarizers. Lvi: Plate-like plagioclase; Lvm: Fine volcanic rock fragments; Q: Quartz. (**a**). The unconformity contact between the Kangkelin and Keziertage formations; (**b**–**d**). The calcareous fine sandstone of the Balikelike Formation from Sample 106-23; (**e**–**g**). The tuffaceous fine lithic sandstone of the Kalundaer Formation from Sample 301-38; (**h**–**j**). Calcareous fine sandy siltstone of the Kalundaer Formation from Sample 301-71. Other legends are shown in Figures 1–3.
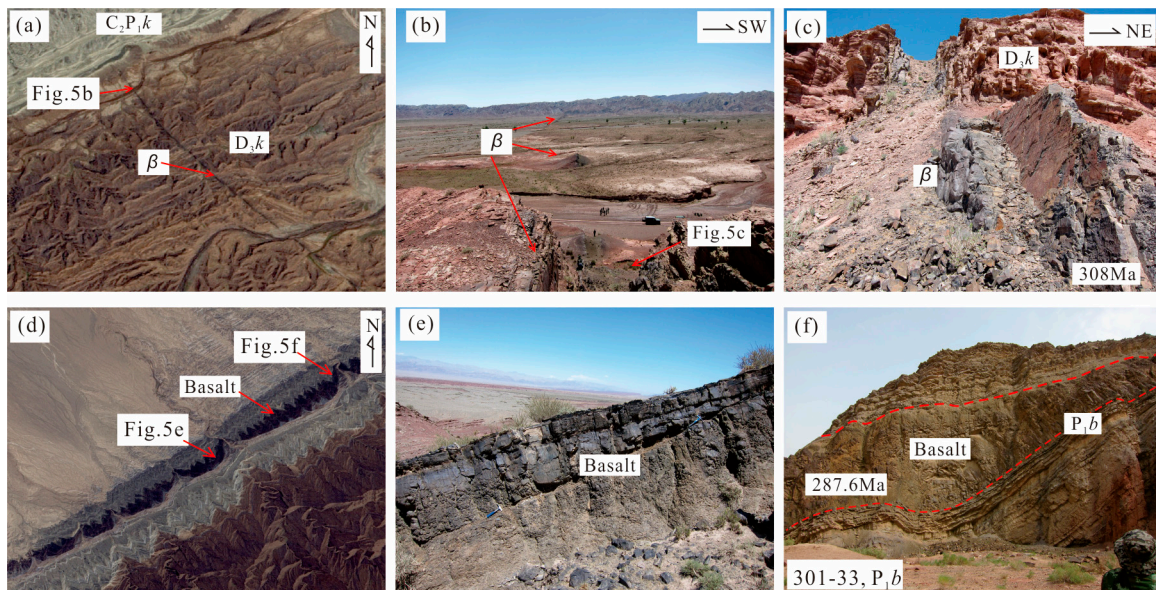
Figure 5. The satellite images (**a**,**d**) and the field photographs (**b**,**c**,**e**,**f**) of the mafic dyke and basalt in the study area. (**a**–**c**) The mafic dyke cut through the Devonian system, covered by the Kangkelin Formation, with an age of 308 Ma: (**d**–**f**) The basalt in the Balikelike Formation, with an age of 287.6 Ma.

3. Samples and Methods

Detrital zircon U-Pb geochronology and geochemical analysis are effective methods to determine sediment provenance and reconstruct the tectonic evolution of adjacent orogens [4,37]. For this purpose, five geochemical samples were collected from the Balikelike Formation (in Section PM301) and sixteen from the Kalundaer Formation (nine samples in Section PM301 and seven in Section PM107). Three detrital zircon samples of the fine-grained calcareous sandstone (B106-23, B301-38, and B301-71) were collected from two sections (Figure 3). Sample B106-23 was collected from the calcareous sandstone of the Balikelike Formation in Section PM106, sample B301-38 was also collected from the tuffaceous fine lithic sandstone of the Kalundaer Formation in Section PM301, and sample B301-71 was also collected from the fine calcareous sandstone of the Kalundaer Formation in Section PM301.

The samples were examined at the State Key Laboratory of Geological Processes and Mineral Resources, China University of Geosciences, in Wuhan. Initially, heavy liquid and magnetic separation techniques were applied to isolate detrital zircons from three calcareous sandstone samples. The obtained zircons were randomly embedded into epoxy resin under a binocular microscope to form sample targets. Subsequently, cathodoluminescence (CL) images of the zircons were acquired using a JXA-8100 scanning electron probe microscope (JEOL, Tokyo, Japan). Zircon U-Pb dating was conducted with a laser ablation inductively coupled plasma mass spectrometer (LA-ICP-MS) equipped with an Agilent 7700 ICP-MS, Santa Clara, CA, USA with a 32 μm laser spot size, 40 mJ/pulse energy density, and 8 Hz rate. The standard GJ-1 zircon was utilized for inter-isotope fractionation calibration, and the standard 91500 was employed to monitor instrument stability. ICPMS-DataCal 10.0 was used to calculate the U-Pb isotope and element concentrations [38–41]. $^{238}U/^{206}Pb$ age data were used for grains younger than 1 Ga, while $^{207}Pb/^{206}Pb$ ages were more desirable for grains older than 10 Ga. IsoplotR was adopted to calculate and plot the concordia diagram and probability histograms [42].

The geochemical samples were analyzed at the State Key Laboratory of Biogeology and Environmental Geology, China University of Geosciences, Wuhan. Whole-rock major elements were analyzed by XRF-1800 with the mixed flux of $45Li_2B_4O_7+10LiBO_2+5LiF$, analytic pure reagents of NH_4NO_3 and $LiBr$. Trace elements were performed by ICP-MS

(Agilent 7700x) (Agilent, Santa Clara, CA, USA). The predecessors have described the test principle and method in detail, and the author will not repeat them [20,24,25].

4. Results

4.1. Detrital Zircon

Detrital zircons from the three samples comprise fragments, short prismatic euhedral, or rounded crystals, ranging in lengths from approximately 100 to 250 μm with width/length ratios of 1:1 to 1:2. In contrast to Precambrian zircons, Paleozoic grains are generally larger and display more prismatic shapes. Based on CL images, most zircons show distinct oscillatory zoning, indicative of a magmatic origin, as supported by their relatively high Th/U ratios (0.2-2). Some zircon grains have experienced subsequent growth stages, forming a bright, narrow rim (Figure 6).
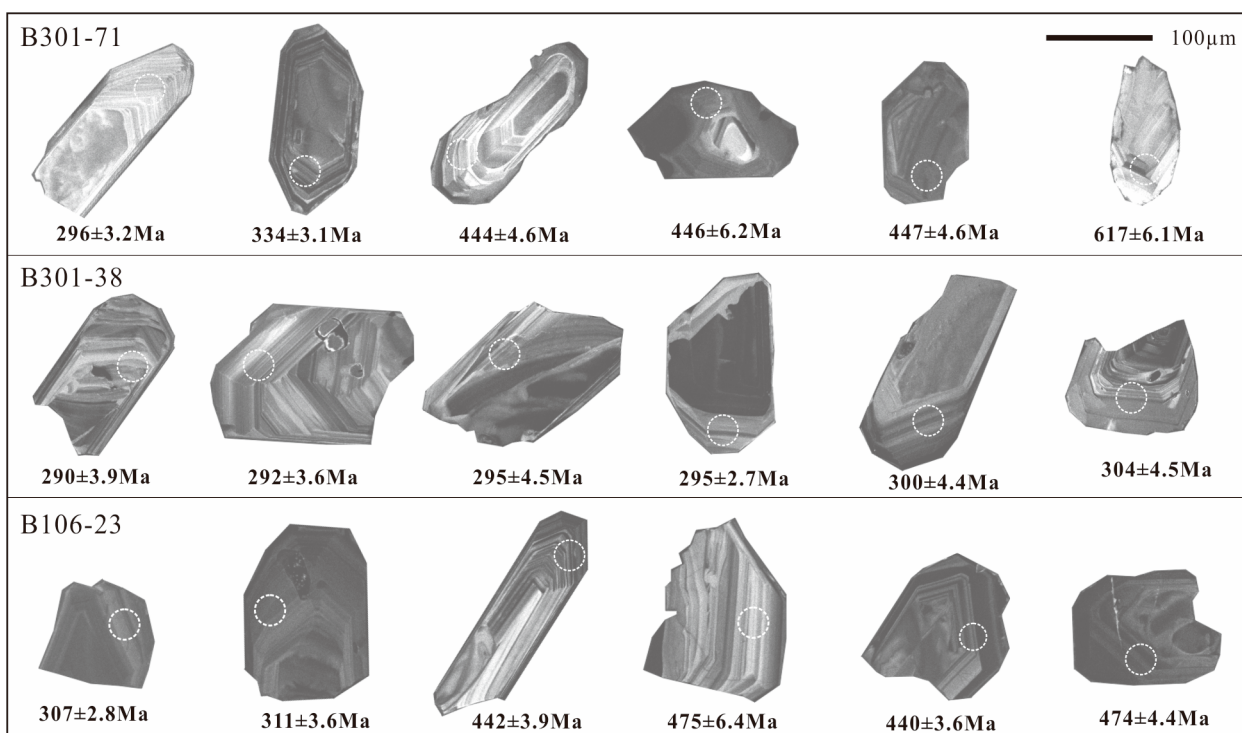

Figure 6. CL images of representative detrital zircons analyzed for U-Pb ages from the Balikelike and Kalundaer formations, NW Tarim. White circles indicate the location of sample spots measured to obtain the U-Pb ages.

A total of 190 zircon grains were analyzed, with 41 analyses excluded due to discordant ages (concordance not within 90% and 110%) or significant signal fluctuations during the analyses. The remaining 149 detrital zircons from the three samples yielded ages ranging from 2632 Ma to 287 Ma. Five groups of $^{206}Pb/^{238}U$ ages were obtained from the detrital zircons of samples B106-23 and B301-71, respectively: 2500~2300 Ma, 2000~1800 Ma, 900~600 Ma, 500–380 Ma and 310–290 Ma (Figure 7a–d). A group of ~295 Ma $^{206}Pb/^{238}U$ ages were obtained from the detrital zircons of sample B301-38 (Figure 7e,f). The detrital zircon U-Pb dating results for all samples are presented in Supplementary Table S1.
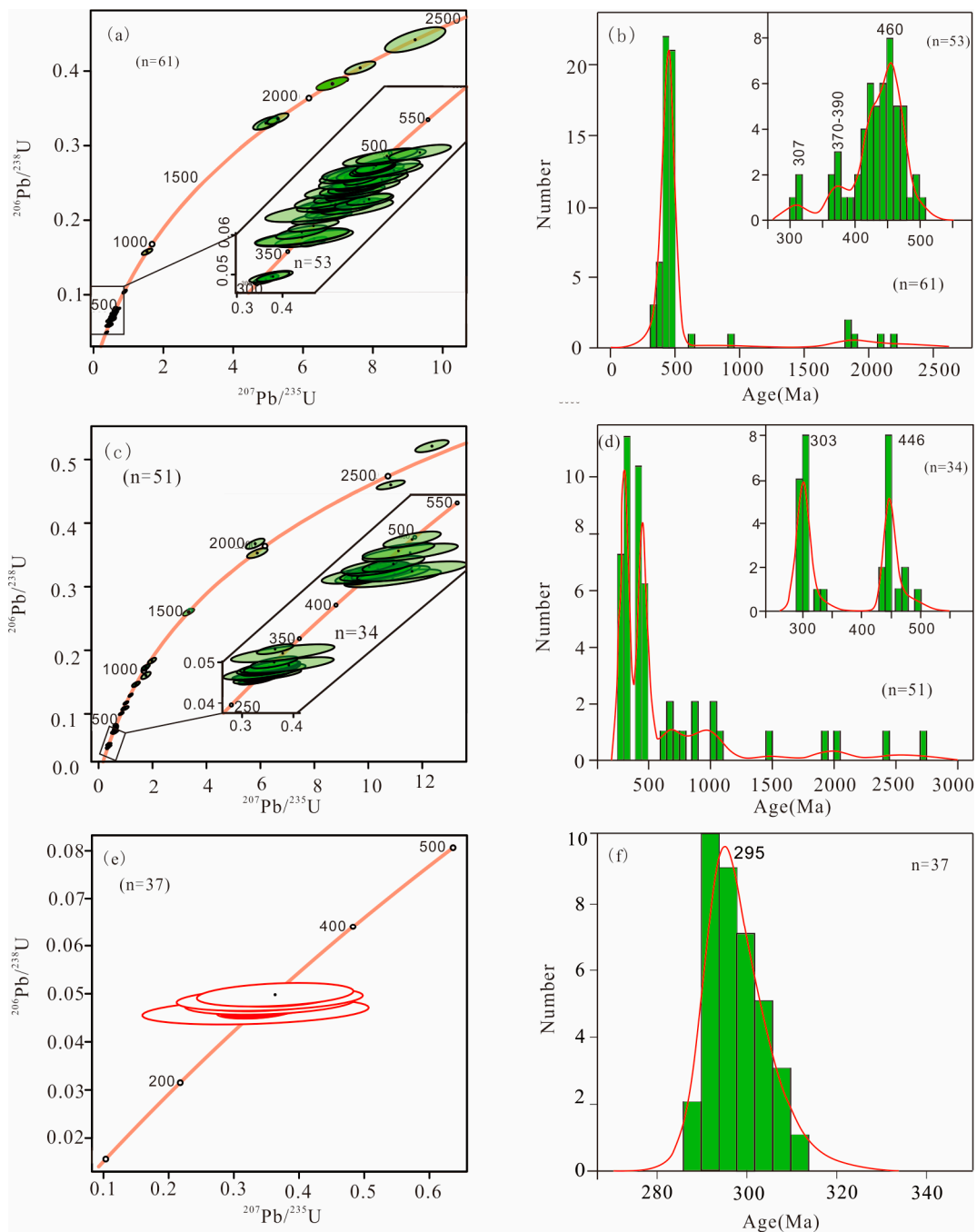
Figure 7. Concordia and histogram-probability density diagrams of detrital zircon U-Pb data for sandstone samples from the Balikelike and Kalundaer formations, NW Tarim. Of all ages, those with more than 10% discordance degrees were excluded. Errors are shown at 1 sigma level. (**a**,**b**) Sample B106-23; (**c**,**d**) Sample B301-38; (**e**,**f**) Sample B301-71.

4.2. Geochemical Characteristics

The bulk chemical composition of turbiditic sandstones and mudstones can effectively indicate environmental characteristics [43,44]. Additionally, the abundance of rare earth elements (REE) and other stable elements (Ti, Zr, Hf, Y, Sc, Nb, Ca, Th, U), or their ratios, have been utilized to d distinguish the tectonic setting of sedimentary basins [44,45]. These elements have intermediate ionic potential and low marine residence times [46,47], and since they are easily incorporated into sediments, they also provide indications of provenance composition [43,44].

4.2.1. Major Elements

This study collected 21 geochemical analysis samples from Section PM301 and Section PM107 in the study area (Figures 1c and 3a,c). The characteristics of the major element contents are shown in Table 1. The results indicate that in the Baliklike Formation sandstone, the SiO_2 content ranges from 53.26% to 77.60%, with an average of 64.91%; Al_2O_3 content ranges from 6.39% to 10.60%, with an average of 8.32%; K_2O+Na_2O content ranges from 2.90% to 4.93%, with a K_2O/Na_2O ratio ranging from 0.34 to 0.87, averaging 0.61; TFe_2O_3+MgO ranges from 1.04% to 4.55%, with an average of 3.12%; CaO content ranges from 2.61% to 16.50%, with an average of 10.17%; MnO averages 0.09%; and P_2O_5 averages 0.03%. In the Kalundaer Formation sandstone, the SiO_2 content ranges from 40.61% to 67.34%, with an average of 54.70%; Al_2O_3 3.85% to 9.62%, with an average of 6.35%; K_2O+Na_2O 1.74% to 8.12%, with K_2O/Na_2O ratios of 0.25 to 0.94, and averaging 0.54; TFe_2O_3+MgO composition spreads from 1.50% to 5.78%, with an average of 3.25%; a CaO content of 6.74% to 28.40%, with an average of 16.96%; MnO averages 0.09%; and P_2O_5 0.05%.

Table 1. The major element concentrations of the sandstones of the Permian Balikelike and Kalundaer formations in the Keping area (*wt.*%).

Sample	SiO_2	Al_2O_3	$Fe_2O_3{}^*$	CaO	MgO	K_2O	Na_2O	TiO_2	P_2O_5	MnO	LOI	Σ
B301-26-1	77.6	8.75	1.69	2.61	1.24	1.15	2.65	0.24	0.03	0.02	3.7	99.68
B301-26-2	64.67	8.29	1.54	10.6	1.36	1.24	2.25	0.2	0.02	0.08	10.09	100.34
B301-27-1	53.26	7.59	1.82	16.5	2.35	1.35	1.55	0.3	0.04	0.09	15.57	100.42
B301-28-1	63.01	6.39	0.41	14.54	0.63	1.42	1.71	0.08	0.01	0.2	12.07	100.47
B301-36-1	66	10.6	3.24	6.6	1.31	1.25	3.68	0.46	0.05	0.06	6.41	99.66
B301-45-1	57.89	6.61	1.7	15.26	1.56	0.88	1.68	0.29	0.06	0.07	13.96	99.96
B301-53-1	60.15	7.64	2.48	12.37	1.87	0.89	2.16	0.5	0.05	0.07	12.19	100.37
B301-58-1	56.87	6.93	2.29	14.88	1.59	1.2	1.83	0.36	0.04	0.06	13.6	99.65
B301-62-1	52.64	6.77	2.25	17.32	1.75	1.26	1.56	0.39	0.04	0.09	15.85	99.92
B301-68-1	58.13	9.62	3.37	10.81	2.41	1.85	1.58	0.44	0.08	0.05	12.08	100.42
B301-71-1	61.86	7.36	1.88	13.38	1.64	1.4	1.58	0.33	0.06	0.06	9.94	99.49
B301-92-1	44.43	4.45	0.98	25.57	1.19	0.9	0.96	0.19	0.04	0.13	21.58	100.42
B301-95-2	59.54	7.82	2.06	6.74	1.53	1.6	6.52	0.38	0.05	0.04	14.25	100.53
B301-102-1	67.34	4.19	0.81	13.28	0.69	0.84	0.93	0.15	0.03	0.07	12.02	100.35
B107-02-1	57.06	7.16	1.82	15.29	1.22	1	2.28	0.3	0.05	0.06	14	100.24
B107-15-1	43.98	5.8	1.88	23.7	1.32	0.69	1.81	0.39	0.08	0.11	19.79	99.55
B107-17-1	52.79	5.6	1.03	19.68	1.13	0.82	1.54	0.19	0.05	0.09	16.75	99.67
B107-22-1	59.77	7.31	2.32	13.13	1.48	1.06	1.95	0.43	0.05	0.06	12.53	100.09
B107-23-1	41.47	4.93	1.53	26.5	1.35	0.55	1.66	0.26	0.04	0.23	21.86	100.38
B107-25-1	60.63	5.51	1.68	14.98	1.14	0.98	1.25	0.25	0.04	0.05	13.15	99.66
B107-25b-1	40.61	3.85	1.06	28.4	1.05	0.51	1.23	0.13	0.04	0.16	23.16	100.2

$Fe_2O_3{}^* = T(Fe_2O_3)$.

4.2.2. Trace Elements

The trace element content (Supplementary Table S2), and trace element ratios (Supplementary Table S3) of the sandstone in the Balikelike and Kalundaer formations have the following characteristics:

The ΣREE content in the sandstones of Balikelike Formation ranges from 77.26 ppm to 231.26 ppm (average 125.55 ppm); LREE/HREE values range from 7.24 to 8.04 (average 8.15); $(La/Yb)_N$ values range from 9.09 to 10.15 (average 10.41); $(La/Sm)_N$ ratios from 3.73 to 3.94 (average 4.04); $(Gd/Yb)_N$ 1.56 to 1.97 (average 1.80); δEu values 0.57 to 1.19 (average 0.61). The ΣREE composition in the Kalundaer sandstones spread from 48.55 ppm to 138.27 ppm (average 98.66 ppm); LREE/HREE ratios from 5.44 to 8.03 (average 7.43); $(La/Yb)_N$ 5.40 to 10.15 (average 10.15); $(La/Sm)_N$ 3.55 to 3.94 (average 3.75); and $(Gd/Yb)_N$ 1.16 to 1.97 (average 1.64); δEu 0.65 to 1.19 (average 0.79).

In the Upper Continental Crust (UCC) normalized multi-element spider diagram (Figure 8a), the large ion lithophile elements (LILE) segment shows significant curve fluctuations. In contrast, the high field strength elements (HFSE) segment exhibits relatively smooth curves. Some large ion lithophile elements (such as Rb, Ba, and Sr) in the Balikelike Formation exhibit significant variations in content, resulting in large fluctuations in the curve; the concentration of these elements in the Kalundaer Formation show relatively minor variations, resulting in smoother curve patterns. Apart from Ti and P, the contents of high field strength elements (such as Zr, Hf, and Yb) do not show significant differences between the two formations, with relatively stable curve patterns. Overall, the variations in REE composition between the two formations are minimal. The chondrite-normalized REE distribution pattern (Figure 8b) reveals that the distribution curves of each sample are parallel, all showing a right-leaning pattern with LREE enrichment and flat HREEs. These characteristics are consistent with the UCC (Figure 8b) [48].
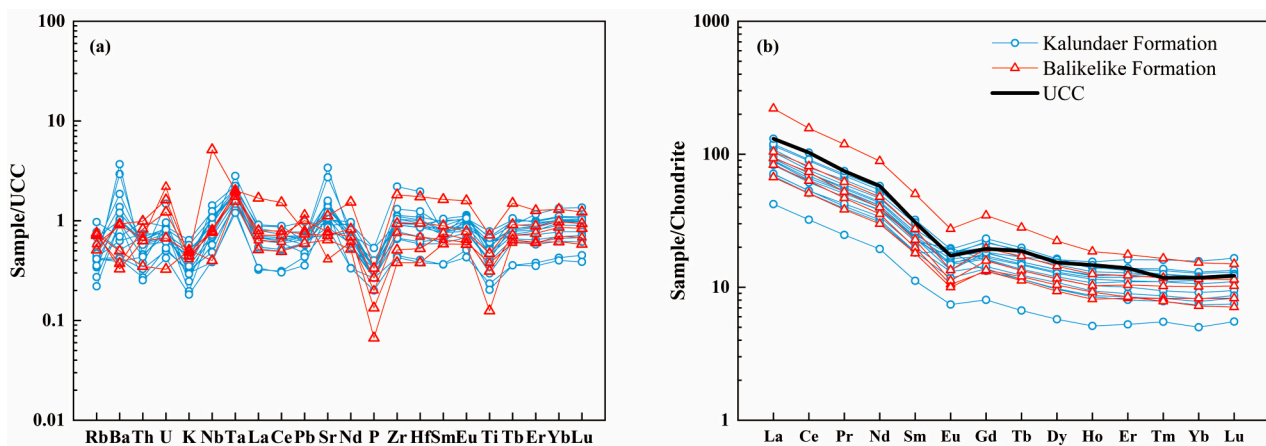

Figure 8. (**a**) UCC-normalized multi-element diagrams for samples of the Balikelike and Kalundaer formations. Normalized to UCC values from Rudnick (2003) [48]; (**b**) chondrite-normalized REE patterns for samples of the Balikelike and Kalundaer formations. Normalized to chondritic values from Taylor (1995) [49]. The standard composition of average UCC after Rudnick (2003) [48] is shown for comparison. (for sample records refer to Supplementary Table S2).

5. Discussion

5.1. Provenance of Precambrian Detrital Zircons

The two samples (B106-23 and B301-71) from the Balikelike and Kalundaer formations exhibit similar Precambrian detrital zircon age distributions, featuring three prominent age groups: 2500~2300 Ma, 2000~1800 Ma, and 900~600 Ma. These ages align closely with the multiphase tectonic-thermal events documented in the history of the Tarim Block. The age population of 2500~2300 Ma corresponds to Late Neoarchean–Early Paleoproterozoic TTG magmatic activity in the Kuruktag uplift, indicating the time of formation of the Tarim Block basement [46–54]. The 2000 Ma to 1800 Ma detrital zircon corresponds to Paleoproterozoic metamorphic and magmatic events during the assembly of the Columbia supercontinent [51–58]. The age groups of 900~600 Ma originate from Neoproterozoic magmatic activity, including mafic dyke swarms, volcanic rocks, ultramafic–mafic intrusions, and granites, which are extensively preserved in the northern Tarim Block [47,59]. Moreover, this age population is regarded as the timing for the breakup of the Tarim Block from Rodinia during the Meso-Neoproterozoic [53,60]. Moreover, these Precambrian zircon grains are characterized by their smaller size and rounded morphology, suggesting they underwent recycling or long-distance transport (Figure 6). Therefore, these Precambrian zircon grains in this study were probably derived from the basement rocks of the Tarim Block, as recorded in the marginal basins of the northwestern Tarim Block, Kuruqtagh, and Aksu areas.

5.2. Provenance of Paleozoic Detrital Zircons

To comprehensively understand the Permian detrital zircon U-Pb ages, we compiled data of 1140 valid detrital zircon U-Pb ages from 14 clastic rocks samples in the Keping area. These data included 991 published zircon U-Pb ages from 11 samples and 149 zircon ages from three samples presented in this paper (Supplementary Table S1). The locations and sample details are provided in Table 2. Specifically, three samples are from the Pennsylvanian to Cisuralian Kangkelin Formation, five from the Cisuralian Kupukuziman Formation, and three from the Early-Guadalupian Kaipaizileike Formation. The Kupukuziman Formation corresponds to the Balikelike Formation, and the Kaipaizileike Formation corresponds to the Kalundaer Formation in this study. These formations are part of the Permian in the Keping area, identified as similar lithostratigraphic units found at various locations.

Table 2. A summary of the sample site, age, lithologies, numbers of U-Pb ages, and reference information of Permian detrital zircon samples in the Keping and adjacent areas.

Samples	Age	Site	Lithology	No. of Valid Ages	Reference
Yg050409	$P_{1-2}ka$	Dawangou section	siltstone	58	[61]
Yg050412	$P_{1-2}ka$	Dawangou section	siltstone	85	[61]
Yg050413	$P_{1-2}ka$	Dawangou section	siltstone	85	[61]
91Si-4	P_1ku	Sishichang section	fine-grained sandstone	92	[62]
SSC03	C_2P_1k	Sishichang section	quartz sandstone	89	[63]
SSC04	C_2P_1k	Sishichang section	quartz sandstone	90	[63]
SSC05	P_1ku *	Sishichang section	coarse sandstone	85	[63]
SSC07	P_1ku	Sishichang section	coarse sandstone	85	[63]
LT7	P_1ku	Subashi section	fine-grained calcareous arenite	92	[17]
LT24B	P_1ku	Linkuangchang section	coarse-fine grained wacke	111	[17]
G8	C_2P_1k	Sishichang section	fine-grained sandstone	119	[64]
BL106-23	P_1b	North Yimugantawu	quartz sandstone	61	This paper
KL301-38	$P_{1-2}k$	South Kepingtage	quartz sandstone	37	This paper
KL301-71	$P_{1-2}k$	South Kepingtage	quartz sandstone	51	This paper

Note: According to the literature [65], the time of the Kaipaizileike Formation ($P_{1-2}ka$) has been revised from Guadalupian to Cisuralian–Guadalupian. * P_1ku—Kupukuziman Formation.

To interpret the potential source of Permian detrital zircons in the Keping area, we compared the detrital zircon U-Pb ages with the Paleozoic crystallization ages (<600 Ma) of magmatic rocks in the YCTB, the STOB, and the northwestern margin of Tarin Block. The ages of magmatic rocks are summarized by Han (2016b) [17], Huang (2018) [66], and Liu (2020) [67] (Figure 9). The Tarim Block and its surrounding blocks experienced frequent tectonic and magmatic activities during the Paleozoic, with ages mainly clustering around 460–390 Ma and 300–270 Ma in the northwestern margin of Tarim Block. These age patterns are similar to those of the STOB, which show major episodes at 300~270 Ma and 450~380 Ma. Additionally, both age patterns correspond to the distribution of detrital zircon U-Pb ages obtained from modern river sands in North Tianshan [68]. However, 380–320 Ma magmatic zircons are lacking in the northwestern margin of Tarin Block and the STOB compared to the YCTB (Figure 9). The dominant age group in the Permian samples consists of many Ordovician to Early Devonian detrital zircons clustering around 500–380 Ma, a prominent feature in the Paleozoic strata of the northwest Tarim Block. For instance, samples from the Late Devonian Kezertage Formation contain numerous detrital zircons with ages ranging from 500–420 Ma [69]. Paleozoic grains are larger than Precambrian zircons, showing more euhedral to subhedral prismatic shapes. CL images indicate that most zircons display clear oscillatory zoning (Figure 6), suggesting a magmatic origin, as supported by their relatively high Th/U ratios (0.2–2). These detrital zircons from Early-Guadalupian sedimentary rocks in the study area likely originated from a magmatic arc.
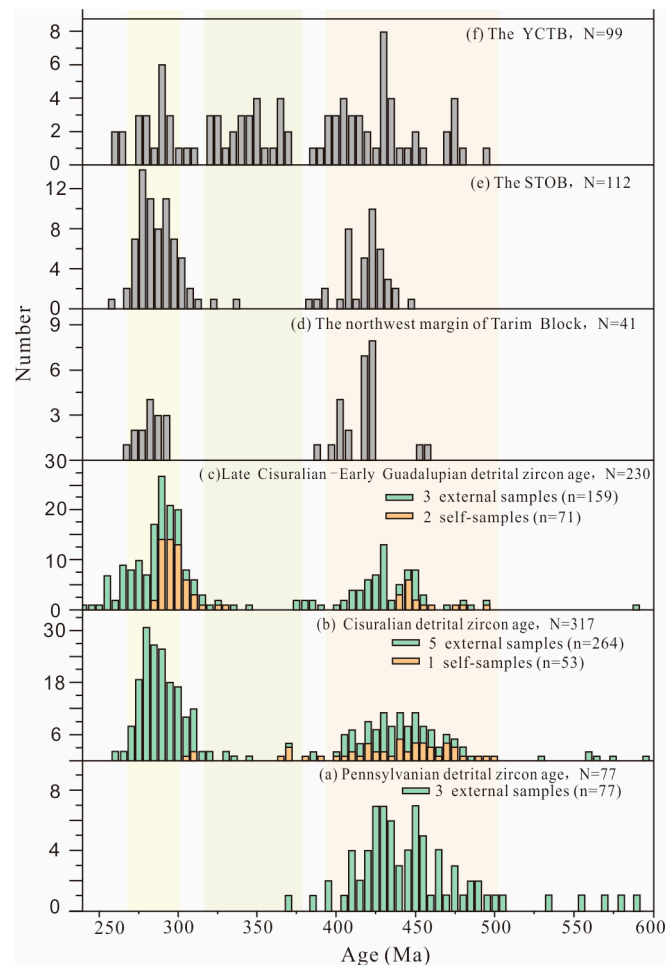
Figure 9. Histogram plots of <600 Ma ages for (**a**–**c**) detrital zircons in the Keping area (for data see Supplementary Tables S1 and S2) and magmatic rocks from (**d**) the northwest margin of the Tarim Block, (**e**) the STOB, and (**f**) the YCTB (data sources: references [17,66,67]).

Tectonic and thermal events were common around the Tarim Block during the Early Paleozoic. The age group of 500~380 Ma correlates with the magmatic belt along the northern margin of Tarin Block, characterized by arc-related granite, granitoids, and diorites formed between 440–380 Ma [18–20,24,32,59,70–73], alongside 433–385 Ma gabbroic pluton [74–76]. These magmatic events may likely provide sources for the Paleozoic zircon. Previous studies have primarily focused on correlating Permian detrital zircons with abundant interbedded basalt rocks in Kupukuziman and Kaipaizileike formations, neglecting specific investigation into the origin of 310–290 Ma zircons [61,77,78].

Detrital zircons aged 310–290 Ma from three samples of the Kaipaizileike Formation show εHf(t) values ranging from −10 to 0, aligning with zircons found in Permian basalt in the Kepingtage area [61]. However, comparing εHf(t) values does not definitively confirm whether the 310–290 Ma detrital zircons were transported from a nearby source. Despite the main magmatic episodes of the Tarim Large Igneous Province (LIP), which include three phases—small-volume kimberlites around ~300 Ma, bimodal magmatism at ~290 Ma, and ~280 Ma [78,79]—evidence of pyroclastic activity predating these episodes has been discovered at the base of the Cisuralian strata. This evidence encompasses tuff layers and tuffaceous sandstone found in the Keping area and the northwestern margin of the Tarin Block [63]. Based on zircon morphology, detrital zircons from the Permian samples display prismatic euhedral shapes, angular roundness, and clear oscillatory zoning, indicating a magmatic origin and slight alteration from external geological processes (Figure 6). This morphology suggests a short-distance sediment transport from the source to the study area.

Sample B301-38 exhibits a single peak zircon age (~295 Ma), further suggesting that these detrital zircons likely originated from a nearby location and underwent rapid deposition (Figure 7e,f). Based on the tectonic setting of the sedimentary basin, these clastic zircons of magmatic origin likely come from the southern Keping forebulge on the south side.

5.3. Provenance and Tectonic Setting

Sedimentary debris is closely related to its source rocks; although the clastic materials undergo some alteration during deposition, the geochemical compositions remain primarily controlled by the source rocks. The chemical components of sandstone can directly reflect the features of the source and its tectonic setting. Usually, geochemical diagrams of sandstones are used to study provenance and tectonic settings [48,80–84].

This article focuses on the geochemical data of samples from the Baliklike and Kalundaer formations and uses the data from previous work to plot partial discrimination maps of the Keping area and its surroundings. The main features are described below.

In the discriminant diagrams of major elements, there is no significant difference in the source areas of the Balikelike and Kalundaer formation sandstones. In the SiO_2-K_2O/Na_2O diagram (Figure 10a), the points are mainly concentrated in the oceanic island arc region, with a few associated with the active continental margin; in the (TFe_2O_3+MgO)-TiO_2 diagram (Figure 10b), the points fall into the continental island arc region and its vicinity, with some points not exhibiting typical characteristics, placed outside of the typical tectonic background field. In the F_3–F_4 diagram (Figure 10c), most samples point to an intermediate igneous provenance, with a few located near the felsic igneous provenance region. The above major element characteristics indicate that the parent rocks of the sandstones from the Balikelike and Kalundaer formations in the study area were generally in an active tectonic setting characteristic of an island arc environment. Although the differences in the discriminant diagrams are not noticeable, compared to the Balikelike Formation, the SiO_2 and Al_2O_3 contents in the sandstones of the Kalundaer Formation tend to decrease, indicating a reduction in compositional maturity. Both have higher K_2O+Na_2O, with K_2O/Na_2O contents averaging 0.54 and 0.61, respectively, indicating a high feldspar composition, containing more plagioclase than potassium feldspar. The TFe_2O_3+MgO concentrations are both low, indicating the minimal presence of ferromagnesian components in the rocks. The corresponding CaO composition in both formations is relatively high, and it is significantly elevated in the Kalundaer than in the Baliklike Formation, pointing to an increasing trend in calcium content. In summary, compared with the Balikelike Formation, the Kalundaer Formation sandstone is constituted of lower compositional maturity, increased calcium content, and decreased stable components such as quartz, suggesting that both may have multiple source characteristics.

In the trace element and REE discrimination diagrams, there is no significant difference in sandstone sample plots from the Balikelike and Kalundaer formations. In the La/Th-Hf diagram (Figure 10d), the points mainly fall in the acidic arc source area, with some points located in the mixed felsic/mafic source area, and only two placed relatively close to the passive margin source area. In the Th-Sc-Zr/10 and La-Th-Sc diagrams (Figure 10e,f), the points mainly plot in the continental island arc area and the angle region between them and the passive continental margin area. Fewer points group with the active continental margin and passive margin source areas, and these tend to lie closer to the continental island arc source.
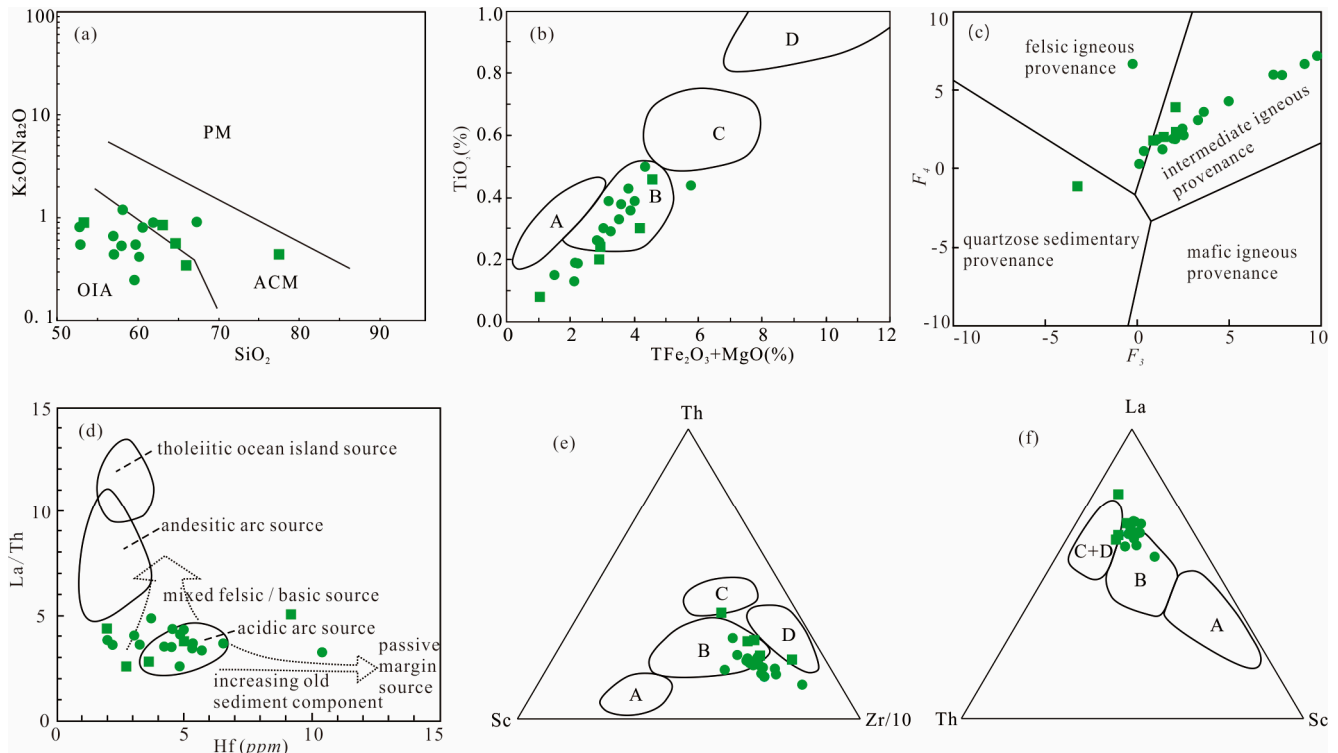
Figure 10. Geochemical discriminant diagrams of sedimentary tectonic setting of Early-Guadalupian (squares are from the Balikelike Formation sandstone; round dots are from the Kalundaer Formation sandstone). (**a**) K_2O/Na_2O–SiO_2 diagram (after Roser (1986) [82]); (**b**) TiO_2–TFe_2O_3+MgO diagram (after Bhatia (1983) [48]); (**c**) F_4–F_3 diagram (after Roser (1988) [83]); (**d**) La/Th–Hf diagram (after Floyd (1987) [81]); (**e**) Th–Sc–Zr/10 diagram (after Bhatia (1986) [80]); (**f**) La–Th–Sc diagram (after Bhatia (1986) [80]). A-Oceanic island arc (OIA); B-continental island arc (CIA); C-active continental margin (ACM); D-passive continental margin (PM).

REEs and trace elements are chemically stable and are less affected by sedimentary environments and diagenetic processes during weathering and transportation. The concentrations and characteristics of REEs in clastic rocks are predominantly controlled by the composition of the source rock area. Consequently, REEs can be used to identify the tectonic setting from which materials were sourced [84]. The ΣREE value in the Balikelike Formation averaged 125.55 ppm, being slightly lower than the 146.4 ppm average of UCC [48], suggesting that the source materials were influenced by intermediate to acidic rocks. The ΣREE value in Kalundaer Formation averaged 98.66 ppm, which is significantly lower than the averaged UCC, indicating a greater contribution from intermediate to acidic rocks to source composition. These characteristics also suggest that during the transition period from the Cisuralian to Guadalupian, volcanic activity in the study area may have intensified.

In the multi-element spider diagrams normalized to UCC (Figure 8a), the REE contents of both formations show little variation. The chondrite-normalized REE patterns (Figure 8b) display a rightward inclination, characterized by enrichment of LREE and depletion of HREE. These characteristics suggest that the sediment sources of the Balikelike and the Kalundaer Formation are essentially stable and homogenous.

Using the geochemical data of Silurian, Devonian, and Mississippian sandstones from the Keping area obtained in previous work for sediment source analysis [69,85,86], in the SiO_2-K_2O/Na_2O diagram (Figure 11a), the Silurian sandstone samples associate with the passive continental margin; the Devonian and Mississippian sandstone samples mainly with the passive continental margin, with a few affiliating with the active continental margin. In the F_3–F_4 discriminant diagram (Figure 11b), most of the Silurian samples were

allocated at the intersection of the quartzose sedimentary and felsic igneous provenance region; the Devonian and Mississippian sample within the quartzose sedimentary source area. In the La/Th-Hf diagram (Figure 11c), the samples mainly assembled in the transitional zone from an acidic arc to a passive margin source. These characteristics suggest that the transition of the sedimentary tectonic setting in the Keping area likely occurred during the Late Devonian to Mississippian Period.
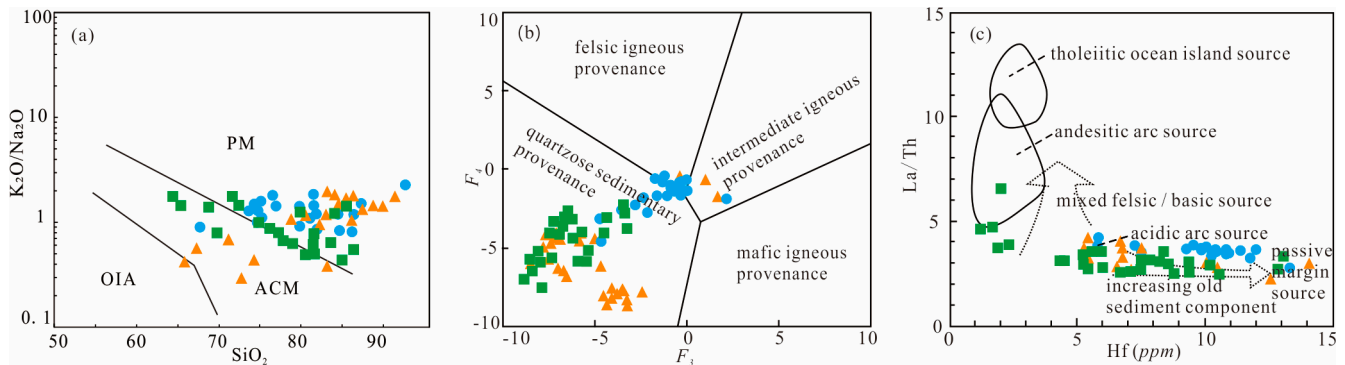

Figure 11. Geochemical discriminant diagrams of the sedimentary tectonic setting from the Silurian to Mississippian. (**a**) K_2O/Na_2O–SiO_2 diagram (after Roser (1986) [82]); (**b**) F_4–F_3 diagram (after Roser (1988) [83]); (**c**) La/Th–Hf diagram (after Floyd (1987) [81]). (Blue round dots are from Silurian samples; brown triangle dots are from Devonian sample; green squares are from Mississippian).

In summary, the tectonic setting of the provenance area for the early to Guadalupian sandstones in the Keping area is characterized by an island arc environment, which underwent significant changes compared to the passive continental margins of the Silurian to Middle Devonian Period. This shift in tectonic background may have occurred from the Late Devonian to the Mississippian, leading to a regional unconformity between the Carboniferous and pre-Carboniferous strata.

5.4. Tectonic Evolution

The tectonic setting of the northwestern margin of Tarin Block was inferred to have been a passive continental margin from the Cambrian to the Silurian. During the Devonian interval, it underwent a gradual transition from a passive continental margin to an island arc setting (Figure 11). In the Early Cambrian, the STO initiated northward subduction beneath the YCTB [87], but the southward subduction was intra-oceanic. Consequently, it did not significantly impact the tectonic setting of the northwest margin of the Tarim Block. The period from the Middle-late Devonian to Early Mississippian is interpreted to represent the time of closure of the STO, during which the sedimentary environment evolved gradually from a residual to a foreland basin. Under subduction accretion, an ocean–continent transition occurred, forming the South Tian Block (STB). Based on geochemical and zircon U-Pb dating data, together with an assessment of field geological conditions (Figure 2), this paper proposes a tectonic evolution model for the Carboniferous to Permian foreland basin in the Keping area, which can be divided into five stages (Figure 12):

1. The Middle-late Devonian to the Early Mississippian, marked the initial development of the foreland basins (the residual marine basin development stage): the sedimentary geological background transitioned from a passive continental to an active continental margin. The study area experienced crustal uplift and erosion, with the emergence of thrust fault activity on the northern side, though a residual marine basin still existed (Figure 12a).

2. The Late Mississippian to the Early Pennsylvanian, was a period of early foreland basin development. The thrust belts had risen to the surface and were subjected to weathering and erosion. In the Aheqi area to the north, wedge-top sediments appeared and developed into the Bashisuogong Formation, which consists of sandstone and

conglomerate, with a small amount of limestone in some areas. Influenced by the YCTB, the study area experienced southward crustal shortening. At this time, foredeep sediments appeared in the Kake area, with the Biegentawu Formation carbonates reaching a thickness of over 1000 m (Figure 12b).

3. The Late Pennsylvanian to the Early Cisuralian, marked the middle foreland basin development stage, when foreland basin development peaked. The foredeep sediments were well-developed and showed a trend of migration to the north. The Kangkelin Formation carbonate, with thicknesses exceeding 1800 m, remained over 900 m thick in the Kake area of the central region. At this time, the Keping area also began to receive deposits, with the Kangkelin Formation reaching a thickness of about 130 m (Figure 12c).

4. The Late Cisuralian was associated with late-stage foreland basin development. It is linked to the emergence of the middle thrust belt, significant migration of foredeep sediments southward, and the appearance of the sedimentary center in the Kake area. The Balikelike Formation had a thickness of over 1000 m, while in the northern, the Aheqi area still measured over 700 m. The Keping area, located in the foreland uplift zone, had a thickness of less than 200 m (Figure 12d).

5. Finally, the Guadalupian transitioned urged in the final stage of foreland basin development. It was characterized by late thrust belts triggering crustal uplift, and the sedimentary environment gradually transformed from a marine-terrestrial interacting setting to a terrestrial environment. In the late stage, terrestrial molasse deposits containing plant fossils emerged, with sediment thickness ranging from approximately 800 to 1300 m in the north and south, showing little difference (Figure 12e).

Also, the Late Guadalupian molasse deposition event subsequently underwent uplift and erosion, with no deposition observed during the Lopingian. The Carboniferous strata on the northwestern margin of the Tarim Block exist in unconformity with the underlying strata, and the strata under the unconformity gradually graduate towards younger deposits from north to south. This relationship suggests that collisional uplift began in the north and progressed southward over time, with its intensity gradually diminishing over time (Figure 2). The closure of the STO likely followed a scissor-like process from east to west during the Middle Devonian to the Early Mississippian [88].

The zircon U-Pb age of mafic dikes intruding the Keziertage Formation and overlain by the Kangkelin Formation is estimated to be 308 Ma (Figures 1b and 5a,b), while the U-Pb age of basalt deposition in the Balikelike Formation approximates 287.6 Ma [36]. These mafic rocks are likely associated with the Cisuralian Tarim Large Igneous Province (LIP), with the 308 Ma mafic dikes possibly representing an early stage of volcanic activity, and the 287.6 Ma basalts a peak in volcanic activity within the province. Additionally, the Cisuralian Tarim LIP provided magmatic zircons to the Kalundaer Formation, with the single peak age of ~295 Ma observed in sample B301-38 serving as evidence. These findings indicate the presence of extensional processes during the development of the foreland basin in the Keping area and provide temporal constraints for the evolution of the foreland basin. The detrital zircon ages of 310–260 Ma indicate the occurrence of co-collision and post-collisional magmatic events after the closure of the STO [87].

The closure of the STO played a key role in the crustal evolution of the northern margin of the Tarim Block during the Late Paleozoic. The latest research shows that the STO continued to subduct northward beneath the YCTB during the Early Devonian [89]. Therefore, this article proposes that the closure of the STO occurred during the Middle Devonian to Early Mississippian, possibly through a soft collision process, without the formation of high mountains. It was mainly characterized by regional crustal uplift and the formation of regional parallel unconformities, with the sedimentary environment transitioning from a residual basin to a foreland basin. During this process, post-collisional extension occurred, forming a series of mafic dikes and basalts. Large-scale crustal uplift and orogeny likely occurred in the Late Guadalupian, evidenced by a set of molasse sediments.
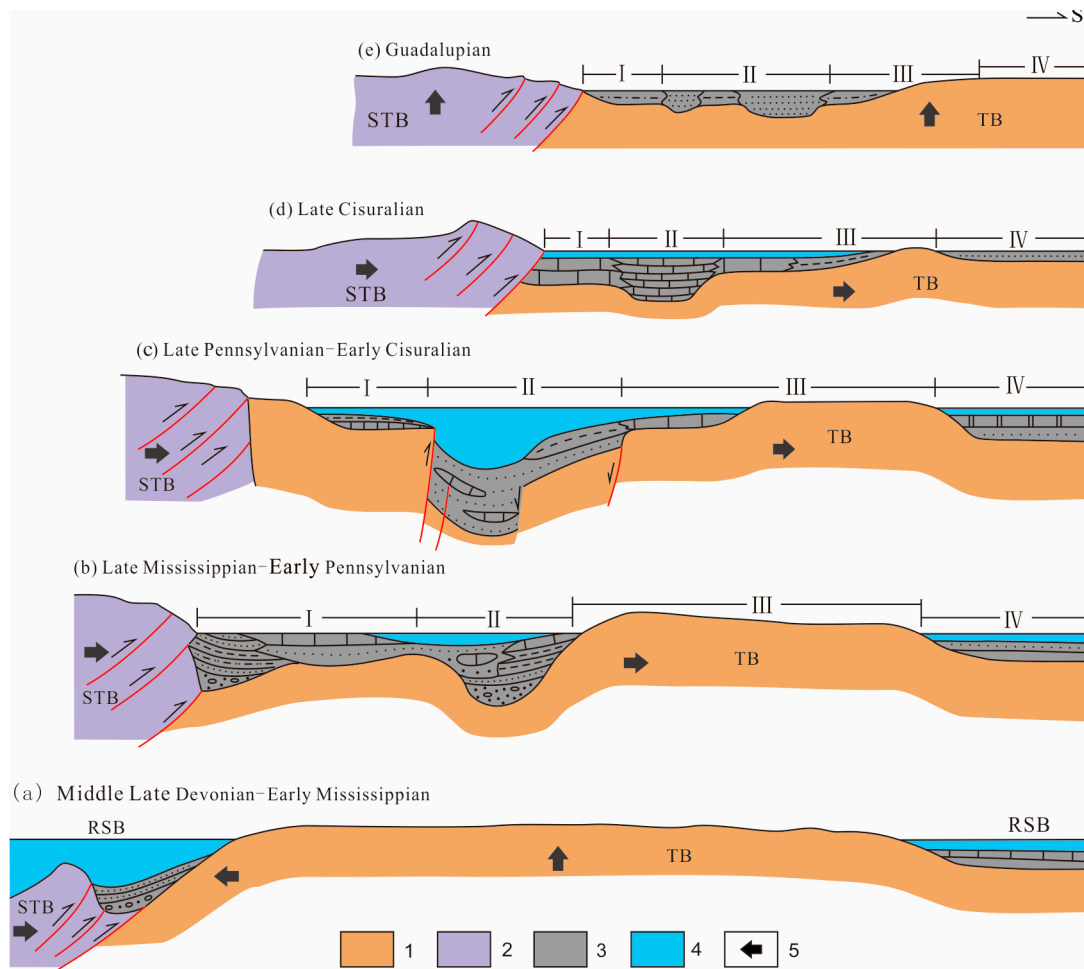
Figure 12. Tectonic evolution model map of the northwest margin of the Tarim Block from the Early-late Devonian to the Guadalupian. (**a**) The period of the initial development of the foreland basins (the residual marine basin development stage); (**b**) The period of early foreland basin development; (**c**) The period of middle foreland basin development stage; (**d**) The late-stage foreland basin development; (**e**) The final stage of foreland basin development. (1. Tarim Block (TB), its pre-Carboniferous strata primarily composed of Silurian and Devonian clastic rocks, Cambrian and Ordovician carbonate rocks, and Precambrian crystalline basement rocks. 2. South Tianshan Block (STB). 3. Foreland basin sediment; 4. Seawater. 5. Direction of crustal movement. I. Wedge top. II. Foredeep. III. Forebulge. IV. Back-bulge. RSB. Remnant sea basin).

6. Conclusions

Previous research evidence, together with the detrital zircon U-Pb geochronology and geochemical data from the Balikelike and Kalundaer formation sandstones in the Keping area, led to the following key conclusions.

1. Five groups of sandstone detrital zircons U-Pb ages were obtained, respectively: 2500–2300 Ma, 2000–1800 Ma, 900–600 Ma, 500–380 Ma, and 310–290 Ma. The Precambrian detrital zircons likely relate to the breakup of the Columbia supercontinent and the assembly of the Rodinia supercontinent. The Paleozoic detrital zircons may have originated from contemporaneous magmatic thermal events. Among them, the ~295 Ma detrital zircons are likely associated with post-collisional extension, representing the activity of the Tarim LIP.
2. Geochemical data analysis indicates that on the northwestern margin of the Tarim Block, the tectonic setting during the Silurian Period was associated with a passive continental margin environment. However, the tectonic setting transformed into a

foreland basin from the Late Mississippian to the Guadalupian. Transformation of the Earth's crustal properties mainly occurred during the Middle-late Devonian to the Early Mississippian, which was also marked when the STO closed. This process likely involved a soft collision, lacking the formation of high mountain ranges, with crustal uplift and orogeny primarily occurring in the Late Guadalupian.

3. The evolution of the foreland basin on the northwest margin of the Tarim Block in the Late Paleozoic can be divided into five stages: (1) the initial stage of foreland basin development from the Middle-late Devonian to the Early Mississippian (residual basin development stage); (2) early stage foreland basin development from the Late Mississippian to the Early Pennsylvanian; (3) middle stage foreland basin development from the Late Pennsylvanian to Early Cisuralian; (4) late stage foreland basin development in the Late Cisuralian; (5) and final stage foreland basin development in the Guadalupian.

References

1. Şengör, A.C.; Natal'in, B.A.; Burtman, V.S. Evolution of the Altaid tectonic collage and Palaeozoic crustal growth in Eurasia. *Nature* **1993**, *364*, 299–307. [CrossRef]
2. Xiao, W.J.; Santosh, M. The western Central Asian Orogenic Belt: A window to accretionary orogenesis and continental growth. *Gondwana Res.* **2014**, *25*, 1429–1444. [CrossRef]
3. Xiao, W.J.; Windley, B.F.; Sun, S.; Li, J.L.; Huang, B.C.; Han, C.M.; Yuan, C.; Sun, M.; Chen, H.L. A Tale of Amalgamation of Three Permo-Triassic Collage Systems in Central Asia: Oroclines, Sutures, and Terminal Accretion. *Annu. Rev. Earth Planet. Sci.* **2015**, *43*, 477–507. [CrossRef]
4. Wang, S.D.; Dai, P.; Zhang, K.X.; Wang, J.X.; Wang, W. Discovery and Sedimentary Sequences of a Special Paleoseamount within the Mazongshan Subduction Accretionary Complex in Beishan Orogen, Gansu Province. *J. Earth Sci.* **2021**, *46*, 215–227. (In Chinese with English Abstract) [CrossRef]
5. Alexeiev, D.V.; Khudoley, A.K.; DuFrane, S.A.; Glorie, S.; Vishnevskaya, I.A.; Semiletkin, S.A.; Letnikova, E.F. Early Neoproterozoic fore-arc basin strata of the Malyi Karatau Range (South Kazakhstan): Depositional ages, provenance and implications for reconstructions of Precambrian continents. *Gondwana Res.* **2023**, *119*, 313–340. [CrossRef]
6. Zhong, L.L.; Wang, B.; Alexeiev, D.V.; Cao, Y.C.; Biske, Y.S.; Liu, H.S.; Zhai, E.Z.; Xing, L.Z. Paleozoic multi-stage accretionary evolution of the SW Chinese Tianshan: New constraints from plutonic complex in the Nalati Range. *Gondwana Res.* **2017**, *45*, 254–274. [CrossRef]
7. Safonova, I.Y.; Santosh, M. Accretionary complexes in the Asia-Pacific region: Tracing archives of Ocean Plate Stratigraphy and tracking mantle plumes. *Gondwana Res.* **2014**, *25*, 126–158. [CrossRef]
8. Safonova, I.; Biske, G.; Romer, R.L.; Seltmann, R.; Simonov, V.; Maruyama, S. Middle Paleozoic mafic magmatism and ocean plate stratigraphy of the South Tianshan, Kyrgyzstan. *Gondwana Res.* **2015**, *413*, 236–256. [CrossRef]
9. Tian, R.S.; Yan, Z.Q.; Xie, G.A. Final subduction-closure process of the Paleo-Asian Ocean in the middle segments of the southern Central Asian Orogenic Belt: Constraints from Permian volcanic rocks and late Triassic mafic dike swarms. *Lithos* **2024**, *488–489*, 107805. [CrossRef]

10. Wakita, K.; Pubellier, M.; Windley, B.F. Tectonic processes, from rifting to collision via subduction, in SE Asia and the western Pacific: A key to understanding the architecture of the Central Asian Orogenic Belt. *Lithosphere* **2013**, *5*, 265–276. [CrossRef]

11. Windley, B.F.; Alexeiev, D.; Xiao, W.J.; Kröner, A.; Badarch, G. Tectonic models for accretion of the Central Asian Orogenic Belt. *J. Geol. Soc.* **2007**, *164*, 31–47. [CrossRef]

12. Han, B.F.; He, G.Q.; Wang, X.C.; Guo, Z.J. Late Carboniferous collision between the Tarim and Kazakhstan-Yili terranes in the western segment of the South Tian Shan Orogen, Central Asia, and implications for the Northern Xinjiang, western China. *Earth-Sci. Rev.* **2011**, *109*, 74–93. [CrossRef]

13. Jiang, T.; Gao, J.; Klemd, R.; Qian, Q.; Zhang, X.; Xiong, X.M.; Wang, X.S.; Tan, Z.; Chen, B.X. Paleozoic ophiolitic mélanges from the South Tianshan Orogen, NW China: Geological, geochemical and geochronological implications for the geodynamic setting. *Tectonophysics* **2014**, *612–613*, 106–127. [CrossRef]

14. Chen, B.; Long, X.; Yuan, C.; Wang, Y.J.; Sun, M.; Xiao, W.J.; Cai, K.D.; Huang, Z.Y. Geochronology and geochemistry of Late Ordovician-Early Devonian gneissic granites in the Kumishi area, northern margin of the South Tianshan Belt: Constraints on subduction process of the South Tianshan Ocean. *J. Asian Earth Sci.* **2015**, *113*, 293–309. [CrossRef]

15. Klemd, R.; Gao, J.; Li, J.L.; Meyer, M. Metamorphic evolution of (ultra)-high-pressure subduction-related transient crust in the South Tianshan Orogen (Central Asian Orogenic Belt): Geodynamic implications. *Gondwana Res.* **2015**, *28*, 1–25. [CrossRef]

16. Han, Y.G.; Zhao, G.C.; Wang, X.C.; Cawood, P.A.; Sun, M.; Eizenhöfer, P.R.; Hou, W.Z.; Zhang, X.R.; Liu, Q. Tarim and North China cratons linked to northern Gondwana through switching accretionary tectonics and collisional orogenesis. *Geology* **2016**, *44*, 95–98. [CrossRef]

17. Han, Y.G.; Zhao, G.C.; Sun, M.; Eizenhöfer, P.R.; Hou, W.Z.; Zhang, X.R.; Liu, Q.; Wang, B.; Liu, D.X.; Xu, B. Late Paleozoic subduction and collision processes during the amalgamation of the Central Asian Orogenic Belt along the South Tianshan suture zone. *Lithos* **2016**, *246–247*, 1–12. [CrossRef]

18. Ge, R.F.; Zhu, W.B.; Wu, H.L.; Zheng, B.H.; Zhu, X.Q.; He, J.W. The Paleozoic northern margin of the Tarim Craton: Passive or active? *Lithos* **2012**, *142–143*, 1–15. [CrossRef]

19. Zhao, Z.Y.; Zhang, Z.C.; Santosh, M.; Huang, H.; Cheng, Z.G.; Ye, J.C. Early Paleozoic magmatic record from the northern margin of the Tarim Craton: Further insights on the evolution of the Central Asian Orogenic Belt. *Gondwana Res.* **2015**, *28*, 328–347. [CrossRef]

20. Wang, M.; Zhang, J.; Zhang, B.; Liu, K.; Ge, M.H. Bi-directional subduction of the South Tianshan Ocean during the Late Silurian: Magmatic records from both the southern Central Tianshan Block and northern Tarim Craton. *J. Asian Earth Sci.* **2016**, *128*, 64–78. [CrossRef]

21. Yang, G.X.; Li, Y.J.; Li, S.Z.; Tong, L.L.; Wang, Z.P.; Wu, L. Accreted seamounts in the South Tianshan Orogenic Belt, NW China. *Geol. J.* **2018**, *53* (Suppl. S2), 16–29. [CrossRef]

22. Alexeiev, D.V.; Biske, Y.S.; Djenchuraeva, A.V.; Kröner, A.; Getman, O.F. Late Carboniferous (Kasimovian) closure of the South Tianshan Ocean: No Triassic subduction. *J. Asian Earth Sci.* **2019**, *173*, 54–60. [CrossRef]

23. Wang, B.; Shu, L.S.; Faure, M.; Jahn, B.-M.; Cluze, D.; Charvet, L.; Chung, S.L.; Meffre, S. Paleozoic tectonics of the southern Chinese Tianshan: Insights from structural, chronological and geochemical studies of the Heiyingshan ophiolitic mélange (NW China). *Tectonophysics* **2011**, *1–4*, 85–104. [CrossRef]

24. Lin, W.; Chu, Y.; Ji, W.B.; Zhang, Z.P.; Shi, Y.H.; Wang, Z.Y.; Li, Z.; Wang, Q.C. Geochronological and geochemical constraints for a middle Paleozoic continental arc on the northern margin of the Tarim block: Implications for the Paleozoic tectonic evolution of the South Chinese Tianshan. *Lithosphere* **2013**, *5*, 355–381. [CrossRef]

25. Ma, X.X.; Shu, L.S.; Meert, J.G.; Li, J.Y. The Paleozoic evolution of Central Tianshan: Geochemical and geochronological evidence. *Gondwana Res.* **2014**, *25*, 797–819. [CrossRef]

26. Loury, C.; Rolland, Y.; Guillot, S.; Mikolaichuk, A.V.; Lanari, P.; Bruguier, O.; Bosch, D. Crustal-scale structure of South Tien Shan: Implications for subduction polarity and Cenozoic reactivation. *Geol. Soc. Lond. Spec. Publ.* **2017**, *SP427*, 197–229. [CrossRef]

27. Gao, J.; Klemd, R.; Qian, Q.; Zhang, X.; Li, J.L.; Jiang, T.; Yang, Y.Q. The collision between the Yili and Tarim blocks of the Southwestern Altaids: Geochemical and age constraints of a leucogranite dike crosscutting the HP-LT metamorphic belt in the Chinese Tianshan Orogen. *Tectonophysics* **2011**, *499*, 118–131. [CrossRef]

28. Xiao, W.J.; Windley, B.F.; Allen, M.B.; Han, C.M. Paleozoic multiple accretionary and collisional tectonics of the Chinese Tianshan orogenic collage. *Gondwana Res.* **2013**, *23*, 1316–1341. [CrossRef]

29. Sang, M.; Xiao, W.J.; Orozbaev, R.; Bakirov, A.; Sakiev, K.; Pak, N.; Ivleva, E.; Zhou, K.F.; Ao, S.J.; Qiao, Q.Q.; et al. Structural styles and zircon ages of the South Tianshan accretionary complex, Atbashi Ridge, Kyrgyzstan: Insights for the anatomy of ocean plate stratigraphy and accretionary processes. *J. Asian Earth Sci.* **2018**, *153*, 9–41. [CrossRef]

30. Chen, X.S.; Lv, A.; Song, H.M.; Liu, L.; Yang, B.Z.; Hou, H.X. Geochemical characteristics and tectonic history of the Silurian sandstones in Akeqi area, Xinjiang. *J. Palaeogeogr.* **2018**, *20*, 271–284. (In Chinese with English Abstract). [CrossRef]

31. Charvet, J.; Shu, L.S.; Laurent-Charvet, S.; Wang, B.; Faure, M.; Cluzel, D.; Chen, Y.; Jong, K. Palaeozoic tectonic evolution of the Tianshan belt, NW China. *Sci. China Earth Sci.* **2011**, *54*, 166–184. [CrossRef]

32. Guo, R.Q.; Qin, Q.; Muhetaer, Z.; Zhao, L.L.; Sun, M.J.; Wei, Z. Geological characteristics and tectonic significance of Ordovician granite intrusions in the western segment of Quruqtagh, Xinjiang. *Earth Sci. Front.* **2013**, *20*, 251–263. (In Chinese with English Abstract)

33. Han, Y.G.; Zhao, G.C.; Sun, M.; Eizenhöfer, P.R.; Hou, W.Z.; Zhang, X.R.; Liu, D.X.; Wang, B. Detrital zircon provenance constraints on the initial uplift and denudation of the Chinese western Tianshan after the assembly of the southwestern Central Asian Orogenic Belt. *Sediment. Geol.* **2016**, *339*, 1–12. [CrossRef]

34. Han, Y.G.; Zhao, G.C.; Sun, M.; Paul, R.; Eizenhöfer, P.R.; Hou, W.Z.; Zhang, X.R.; Liu, D.X.; Wang, B.; Zhang, G.W. Paleozoic accretionary orogenesis in the Paleo-Asian Ocean: Insights from detrital zircons from Silurian to Carboniferous strata at the northwestern margin of the Tarim Craton. *Tectonics* **2015**, *34*, 334–351. [CrossRef]

35. Xia, J.K.; Hou, G.T.; Zhong, Z.Q.; Li, X.; Chang, H.N.; Wei, L.Y.; Wu, S.X. Using detrital zircons to constrain the late Paleozoic tectonic evolution of the adjacent tectonic domains of the Tarim Craton, NW China. *J. Asian Earth Sci.* **2024**, *267*, 106138. [CrossRef]

36. Dai, Y.X.; Zhang, X.Y.; Yan, K.; Li, L.L.; Yang, B.Z.; Zhao, Z.G.; Zhou, Q.; Sun, Z.L.; Wang, B.; Gao, H. Zircon U-Pb Chronology, Geochemical Characteristics of the Early Permian Basalt in the Keping Area, Xinjiang and Their Geological Significance. *Geol. Sci. Technol. Inf.* **2017**, *36*, 1–13. (In Chinese with English Abstract)

37. Yang, J.H.; Cawood, P.A.; Du, Y.S.; Huang, H.; Huang, H.W.; Tao, P. Large Igneous Province and magmatic arc sourced Permian-Triassic volcanogenic sediments in China. *Sediment. Geol.* **2012**, *261–262*, 120–131. [CrossRef]

38. Liu, Y.S.; Hu, Z.C.; Zong, K.Q.; Gao, C.G.; Gao, S.; Xu, J.; Chen, H.H. Reappraisement and refinement of zircon U-Pb isotope and trace element analyses by LA-ICP-MS. *Chin. Sci. Bull.* **2010**, *55*, 1535–1546. [CrossRef]

39. Chen, L.; Liu, Y.S.; Hu, Z.C.; Gao, S.; Zong, K.Q.; Chen, H.H. Accurate determinations of fifty-four major and trace elements in carbonate by LA-ICP-MS using normalization strategy of bulk components as 100%. *Chem. Geol.* **2011**, *284*, 283–295. [CrossRef]

40. Hu, Z.C.; Liu, Y.S.; Gao, S.; Liu, W.G.; Yang, L.; Zhang, W.; Tong, X.R.; Lin, L.; Zong, K.Q.; Li, M.; et al. Improved in situ Hf isotope ratio analysis of zircon using newly designed X skimmer cone and Jet sample cone in combination with the addition of nitrogen by laser ablation multiple collector ICP-MS. *J. Anal. At. Spectrom.* **2012**, *27*, 1391–1399. [CrossRef]

41. Lin, J.; Liu, Y.S.; Yang, Y.H.; Hu, Z.C. Calibration and correction of LA-ICP-MS and LA-MC-ICP-MS analyses for element contents and isotopic ratios. *Solid Earth Sci.* **2016**, *1*, 5–27. [CrossRef]

42. Vermeesch, P. IsoplotR: A free and open toolbox for geochronology. *Geosci. Front.* **2018**, *9*, 1479–1493. [CrossRef]

43. Bhatia, M.R. Plate Tectonics and Geochemical Composition of Sandstones. *J. Geol.* **1983**, *91*, 611–627. [CrossRef]

44. Bhatia, M.R. Rare earth element geochemistry of Australian Paleozoic graywackes and mudrocks: Provenance and tectonic control. *Sediment. Geol.* **1985**, *45*, 97–113. [CrossRef]

45. Bhatia, M.R.; Taylor, S.R. Trace-element geochemistry and sedimentary provinces: A study from the Tasman Geosyncline, Australia. *Chem. Geol.* **1981**, *33*, 115–125. [CrossRef]

46. Henderson, P. *Inorganic Geochemistry*; Pergamon Press: Oxford, UK, 1982.

47. Mason, B.; Moore, C.B. *Principles of Geochemktry*; Wiley & Sons: Hoboken, NJ, USA, 1982; pp. 212–220.

48. Rudnick, R.; Gao, S. Composition of the continental crust. In *The Crust, Treatise on Geochemistry*; Rudnick, R., Ed.; Elsevier: Amsterdam, The Netherlands, 2003; Volume 3, pp. 1–64. [CrossRef]

49. Taylor, S.R.; McLennan, S.M. The geochemical evolution of the continental crust. *Rev. Geophys.* **1995**, *33*, 241. [CrossRef]

50. Long, X.P.; Yuan, C.; Sun, M.; Zhao, G.C.; Xiao, W.J.; Wang, Y.J.; Yang, Y.H.; Hu, A.Q. Archean crustal evolution of the northern Tarim craton, NW China: Zircon U–Pb and Hf isotopic constraints. *Precambrian Res.* **2010**, *180*, 272–284. [CrossRef]

51. Shu, L.S.; Deng, X.L.; Zhu, W.B.; Ma, D.S.; Xiao, W.J. Precambrian tectonic evolution of the Tarim Block, NW China: New geochronological insights from the Quruqtagh domain. *J. Asian Earth Sci.* **2011**, *42*, 774–790. [CrossRef]

52. Zhang, C.L.; Li, H.K.; Santosh, M.; Li, Z.X.; Zou, H.B.; Wang, H.Y.; Ye, H.M. Precambrian evolution and cratonization of the Tarim Block, NW China: Petrology, geochemistry, Nd-isotopes and U-Pb zircon geochronology from Archaean gabbro-TTG-potassic granite suite and Paleoproterozoic metamorphic belt. *J. Asian Earth Sci.* **2012**, *47*, 5–20. [CrossRef]

53. Ma, X.X.; Shu, L.S.; Jahn, B.-M.; Zhu, W.B.; Faure, M. Precambrian tectonic evolution of Central Tianshan, NW China: Constraints from U-Pb dating and in situ Hf isotopic analysis of detrital zircons. *Precambrian Res.* **2012**, *222–223*, 450–473. [CrossRef]

54. Konopelko, D.; Biske, Y.S.; Kullerud, K.; Ganiev, I.; Seltmann, R.; Brownscombe, W.; Mirkamalov, R.; Wang, B.; Safonova, I.; Kotler, P.; et al. Early Carboniferous metamorphism of the Neoproterozoic South Tien Shan-Karakum basement: New geochronological results from Baisun and Kyzylkum, Uzbekistan. *J. Asian Earth Sci.* **2019**, *177*, 275–286. [CrossRef]

55. Ge, R.F.; Zhu, W.B.; Wu, H.L.; He, J.W.; Zheng, B.H. Zircon U-Pb ages and Lu-Hf isotopes of Paleoproterozoic metasedimentary rocks in the Korla Complex, NW China: Implications for metamorphic zircon formation and geological evolution of the Tarim Craton. *Precambrian Res.* **2013**, *231*, 1–18. [CrossRef]

56. Zhang, J.X.; Yu, S.Y.; Gong, J.H.; Li, H.K.; Hou, K.J. The latest Neoarchean-Paleoproterozoic evolution of the Dunhuang block, eastern Tarim craton, northwestern China: Evidence from zircon U-Pb dating and Hf isotopic analyses. *Precambrian Res.* **2013**, *226*, 21–42. [CrossRef]

57. Zhu, W.B.; Zheng, B.H.; Shu, L.S.; Ma, D.S.; Wu, H.L.; Li, Y.X.; Huang, W.T.; Yu, J.J. Neoproterozoic tectonic evolution of the Precambrian Aksu blueschist terrane, northwestern Tarim, China: Insights from LA-ICP-MS zircon U-Pb ages and geochemical data. *Precambrian Res.* **2011**, *185*, 215–230. [CrossRef]

58. Lei, R.X.; Wu, C.Z.; Chi, G.X.; Chen, C.; Gu, L.X.; Jiang, Y.H. Petrogenesis of the Palaeoproterozoic Xishankou pluton, northern Tarim block, northwest China: Implications for assembly of the supercontinent Columbia. *Int. Geol. Rev.* **2012**, *54*, 1829–1842. [CrossRef]

59. Ge, R.F.; Zhu, W.B.; Wilde, S.A.; He, J.W.; Cui, X.; Wang, X.; Zheng, B.H. Neoproterozoic to Paleozoic long-lived accretionary orogeny in the northern Tarim Craton. *Tectonics* **2014**, *33*, 302–329. [CrossRef]

60. Wang, X.S.; Klemd, R.; Gao, J.; Jiang, T.; Li, J.L.; Xue, S.C. Final assembly of the southwestern Central Asian Orogenic Belt as constrained by the evolution of the South Tianshan Orogen: Links with Gondwana and Pangea. *J. Geophys. Res. Solid Earth* **2018**, *123*, 7361–7388. [CrossRef]

61. Zou, S.Y.; Li, Z.L.; Ren, Z.Y.; Li, Y.Q.; Yang, S.F.; Chen, H.L.; Song, B.; Yu, X. U-Pb dating and Hf isotopic compositions of detrital zircons from Permian sedimentary rocks in Keping area of Tarim Basin, Xinjiang, China: Constraints on geological evolution of Tarim Block. *Acta Petrol. Sin.* **2013**, *29*, 3369–3388. (In Chinese with English Abstract)

62. Carroll, A.R.; Dumitru, T.A.; Graham, S.A.; Hendrix, M.S. An 800 million-year detrital zircon record of continental amalgamation: Tarim basin, NW China. *Int. Geol. Rev.* **2013**, *55*, 818–829. [CrossRef]

63. Li, Z.; Gao, J.; Guo, C.T.; Xu, J.Q. Devonian-Carboniferous tectonic evolution of continental margins in northern Tarim block, Northwest China: Constrained by basin-fill sequences and provenance systems. *Earth Sci. Front.* **2015**, *22*, 35–52. (In Chinese with English Abstract) [CrossRef]

64. Guo, C.T.; Gao, J.; Li, Z. Depositional and provenance records of Lower Permian and stones from Sishichang area, northwestern Tarim Basin: Implications for tectonic evolution. *J. Earth Sci.* **2018**, *43*, 4149–4168. (In Chinese with English Abstract). [CrossRef]

65. Li, H.Y.; Huang, X.L.; Li, W.X.; Cao, J.; He, P.L.; Xu, Y.G. Age and geochemistry of the Early Permian basalts from Qimugan in the southwestern Tarim basin. *Acta Petrol. Sin.* **2013**, *29*, 3353–3368. (In Chinese with English Abstract).

66. Huang, H.; Cawood, P.A.; Ni, S.; Hou, M.C.; Shi, Z.Q.; Hu, X.L. Provenance of late Paleozoic strata in the Yili Basin: Implication for the South Tianshan orogenic belt. *Geol. Soc. Am. Bull.* **2018**, *130*, 952–974. [CrossRef]

67. Liu, G.P.; Jiang, B.; Guo, R.Q.; Gong, X.K.; Guo, M.; Cui, T. U–Pb age and Hf isotopic composition of detrital zircons from the modern river of the South Tianshan orogenic belt and their implications for Palaeozoic tectonic and crustal evolution. *Geol. J.* **2020**, *55*, 7114–7131. [CrossRef]

68. Ren, R.; Guan, S.W.; Han, B.F.; Su, L. Chronological constraints on the tectonic evolution of the Chinese Tianshan Orogen through detrital zircons from modern and palaeo-river sands. *Int. Geol. Rev.* **2017**, *59*, 1657–1676. [CrossRef]

69. Yan, K.; Li, W.; Sun, J.G.; Yang, B.Z.; Li, X.Y.; Su, J. Provenance and Tectonic Significance of the Sandstone in Devonian Keziertage Formation in Keping, Xinjiang. *Geol. Sci. Technol. Inf.* **2017**, *36*, 7–17. (In Chinese with English Abstract)

70. Wang, C.; Luo, J.H.; Che, Z.C.; Liu, L.; Zhang, J.Y. Geochemical characteristics and U-Pb LA-ICP-MS zircon dating of the Oxidaban pluton from Xinjiang, China: Implications for a Paleozoic oceanic subduction process in southwestern Tianshan. *Acta Geol. Sin.* **2009**, *83*, 272–283. (In Chinese with English Abstract). [CrossRef]

71. Guo, R.Q.; Qin, Q.; Zhang, X.F.; Sun, B.S.; Guo, Y. Geochronology, Petrogeochemistry of Western-Kuoktagh Alkaline Rocks in Quruqtagh Area in Xinjiang and Its Geological Implications. *J. Jilin Univ. (Earth Sci. Ed.)* **2013**, *43*, 457–468. (In Chinese with English Abstract) [CrossRef]

72. Huang, H.; Zhang, Z.Z.; Santosh, M.; Zhang, D.Y.; Zhao, Z.D.; Liu, J.L. Early Paleozoic Tectonic Evolution of the South Tianshan Collisional Belt: Evidence from Geochemistry and Zircon U-Pb Geochronology of the Tie'reke Monzonite Pluton, Northwest China. *J. Geol.* **2013**, *121*, 401–424. [CrossRef]

73. Jia, X.L.; Guo, R.Q.; Chai, F.M. Geochemistry and geochronology of monzogranites in Kuruktag of Xinjiang and their tectonic implications. *Geol. Bull. China* **2013**, *32*, 239–250. (In Chinese with English Abstract). [CrossRef]

74. Qin, Q.; Huang, H.; Wang, T.; Guo, R.Q.; Zhang, Z.C.; Tong, Y. Relationship of the Tarim Craton to the Central Asian Orogenic Belt: Insights from Devonian intrusions in the northern margin of Tarim Craton, China. *Int. Geol. Rev.* **2016**, *58*, 2007–2028. [CrossRef]

75. Guo, R.Q.; Qin, Q.; Zou, M.Y.; Liang, W.B. Geochronology, petrogeochemical characteristics and tectonic significance of gabbro dike from western Quruqtagh in Xinjiang. *Northwestern Geol.* **2018**, *51*, 70–81. (In Chinese with English Abstract) [CrossRef]

76. Liang, W.B.; Guo, R.Q.; Liu, G.P.; Zou, M.Y.; Hu, X.Y.; Wu, H.N.; Zhang, M.D.; Cui, T. LA-ICP-MS zircon U-Pb age and geochemistry of the olivine gabbro dike in the western segment of Kuruktag, Xinjiang and its tectonic significance. *Geol. Sci. Technol. Inf.* **2019**, *38*, 58–67. (In Chinese with English Abstract) [CrossRef]

77. Li, J.Y.; Liu, J.F.; Zheng, G.R.; Feng, Q.W.; Zheng, P.X.; Zhu, Z.X.; Wang, L.J.; Zhang, X.W.; Song, B. The eruptive timing of Permian basalts in Keping area, the northwest margin of Tarim Basin, China: Evidence from detrital zircons. *J. Earth Sci. Environ.* **2017**, *39*, 301–325. (In Chinese with English Abstract) [CrossRef]

78. Zhang, D.Y.; Zhou, T.F.; Yuang, F.; Fan, Y.; Liu, S.; Du, H.X. LA-ICPMS U-Pb ages Hf isotope characteristics of zircons from basalt in the Kupukuziman Formation Keping area Tarim Basin. *Acta Petrol. Sin.* **2010**, *26*, 963–974. (In Chinese with English Abstract).

79. Xu, Y.G.; Wei, X.; Luo, Z.Y.; Liu, H.Q.; Cao, J. The Early Permian Tarim Large Igneous Province: Main characteristics and a plume incubation model. *Lithos* **2014**, *204*, 20–35. [CrossRef]

80. Bhatia, M.R.; Crook, K.A.W. Trace element characteristics of graywackes and tectonic setting discrimination of sedimentary basins. *Contrib. Mineral. Petrol.* **1986**, *92*, 181–193. [CrossRef]

81. Floyd, P.A.; Leveridge, B.E. Tectonic environment of the Devonian Gramscatho basin, south Cornwall: Framework mode and geochemical evidence from turbiditic sandstones. *J. Geol. Soc.* **1987**, *144*, 531–542. [CrossRef]

82. Roser, B.P.; Korsch, R.J. Determination of tectonic setting of sandstone-mudstone suites using SiO_2 content and K_2O/Na_2O ratio. *J. Geol.* **1986**, *94*, 635–650. [CrossRef]

83. Roser, B.P.; Korsch, R.J. Provenance signatures of sandstone mudstone suites determined using discriminant function analysis of major-element data. *Chem. Geol.* **1988**, *67*, 119–139. [CrossRef]

84. McLennan, S.M.; Hemming, S.; McDaniel, D.K.; Hanson, G.N. Geochemical approaches to sedimentation, provenance, and tectonics. In *Processes Controlling the Composition of Clastic Sediments*; Johnsson, M.J., Basu, A., Eds.; Geological Society of America: Boulder, CO, USA, 1993; pp. 21–40. [CrossRef]

85. Li, L.L.; Yang, B.Z.; Yin, Y.H.; Liu, L.L.; Wang, B. Provenance Analysis from Early Silurian Kepingtage Formation in Keping Area, Xinjiang: Constraints from Geochemical Characteristics and Zircon U-Pb Geochronology. *Geol. Sci. Technol. Inf.* **2017**, *36*, 1–12. (In Chinese with English Abstract)

86. Luo, Y.J.; Wang, B.; Wang, G.C.; Chen, B.; Zhang, H.D.; Ma, B.Y. Provenance and Tectonic Environment of Lower Devonian Apadalkan Formation in Southwest Tianshan. *J. Earth Sci.* **2022**, *2*, 1–21. (In Chinese with English Abstract)

87. Liu, G.P.; Cheng, Y.F.; Guo, R.Q.; Wei, Z.; Sun, J.M.; Gong, X.K. U-Pb and Hf isotopes of detrital zircon in sediments from Wulasitai River in Xinjiang and its geological significance. *Chin. J. Geol.* **2024**, *59*, 466–483. (In Chinese with English Abstract)

88. Li, P.; Zhu, T.; Lv, P.R.; Wang, H.L.; Chen, J.L. Early Cambrian Xiate Gabbro in Western Tianshan: Magmatic Records of Initial Subduction of the South Tianshan Ocean. *Northwest. Geol.* **2024**, *57*, 44–58. (In Chinese with English Abstract)

89. Tian, H.; Liu, X.J.; Liu, X.; Liu, P.D.; Song, Y.J.; Xiao, Y.; Zhang, Z.G. Magmatism of the Oceanic Continental Arc in the Southern Tianshan, Xinjiang: Constrain from the Geochemistry and Lu-Hf Isotopes Study of the Early Devonian Wuwamen Volcanic Rocks. *Geotecton. Metallog.* **2024**. (In Chinese with English Abstract) [CrossRef]